Article

Structural and developmental principles of neuropil assembly in *C. elegans*

https://doi.org/10.1038/s41586-020-03169-5

Received: 21 April 2020

Accepted: 12 November 2020

Published online: 24 February 2021

Check for updates

Mark W. Moyle[1], Kristopher M. Barnes[2], Manik Kuchroo[3], Alex Gonopolskiy[3], Leighton H. Duncan[1], Titas Sengupta[1], Lin Shao[1], Min Guo[4], Anthony Santella[2], Ryan Christensen[4], Abhishek Kumar[5], Yicong Wu[4], Kevin R. Moon[6], Guy Wolf[7], Smita Krishnaswamy[3,10], Zhirong Bao[2,10], Hari Shroff[4,5,10], William A. Mohler[8,10] & Daniel A. Colón-Ramos[1,5,9,10]✉

Neuropil is a fundamental form of tissue organization within the brain[1], in which densely packed neurons synaptically interconnect into precise circuit architecture[2,3]. However, the structural and developmental principles that govern this nanoscale precision remain largely unknown[4,5]. Here we use an iterative data coarse-graining algorithm termed 'diffusion condensation'[6] to identify nested circuit structures within the *Caenorhabditis elegans* neuropil, which is known as the nerve ring. We show that the nerve ring neuropil is largely organized into four strata that are composed of related behavioural circuits. The stratified architecture of the neuropil is a geometrical representation of the functional segregation of sensory information and motor outputs, with specific sensory organs and muscle quadrants mapping onto particular neuropil strata. We identify groups of neurons with unique morphologies that integrate information across strata and that create neural structures that cage the strata within the nerve ring. We use high resolution light-sheet microscopy[7,8] coupled with lineage-tracing and cell-tracking algorithms[9,10] to resolve the developmental sequence and reveal principles of cell position, migration and outgrowth that guide stratified neuropil organization. Our results uncover conserved structural design principles that underlie the architecture and function of the nerve ring neuropil, and reveal a temporal progression of outgrowth—based on pioneer neurons—that guides the hierarchical development of the layered neuropil. Our findings provide a systematic blueprint for using structural and developmental approaches to understand neuropil organization within the brain.

To elucidate the structural and developmental principles that govern neuropil assembly, we examined the *C. elegans* nerve ring neuropil, a major site of neuronal integration that contains 181 of the 282 somatic neurons in the adult hermaphrodite[3]. The lineage, morphology and synaptic connectivity of all 181 neurons is known[3,11]. Network principles and circuit motifs[12–20] as well as cellular and molecular mechanisms of nerve ring formation[21–24] have been elucidated. However, we lack an understanding of the structural design principles that underlie the architecture and function of the nerve ring neuropil, and the developmental sequence that forms this functional structure.

Quantitative analyses of neuropil organization

To systematically dissect the organization of the nerve ring neuropil, we analysed previously segmented data[18,19] in which more than 100,000 instances of neurite–neurite contacts had been quantified for two published *C. elegans* electron microscopy neuropil datasets[3] (Fig. 1a). We focused on contact profiles instead of synaptic connections to reveal both functional and structural neuropil relationships.

We generated an adjacency matrix by summing all contact surface areas for each possible neuron pair, and applied a new diffusion condensation[6] (DC) clustering algorithm to iteratively cluster neurons on the basis of the quantitative similarity of the contact profile of each neuron (Fig. 1a). Unlike other clustering algorithms[25–27], diffusion condensation condenses data without assuming underlying data structure or forcing a *k*-way partition. At each iteration, diffusion condensation clusters the data by merging neurons that are within a threshold distance of each other. We then applied C-PHATE, an extension of the PHATE[28] visualization method, to generate an interactive 3D visualization of the iterative diffusion condensation clustering (Fig. 1a, b,

[1]Department of Neuroscience and Department of Cell Biology, Yale University School of Medicine, New Haven, CT, USA. [2]Developmental Biology Program, Sloan Kettering Institute, New York, NY, USA. [3]Department of Genetics, Yale University School of Medicine, New Haven, CT, USA. [4]Laboratory of High Resolution Optical Imaging, National Institute of Biomedical Imaging and Bioengineering, National Institutes of Health, Bethesda, MD, USA. [5]Marine Biological Laboratory, Woods Hole, MA, USA. [6]Department of Mathematics and Statistics, Utah State University, Logan, UT, USA. [7]Department of Mathematics and Statistics, Université de Montréal, Montreal, Quebec, Canada. [8]Department of Genetics and Genome Sciences and Center for Cell Analysis and Modeling, University of Connecticut Health Center, Farmington, CT, USA. [9]Instituto de Neurobiología, Recinto de Ciencias Médicas, Universidad de Puerto Rico, San Juan, Puerto Rico. [10]These authors jointly supervised this work: Smita Krishnaswamy, Zhirong Bao, Hari Shroff, William A. Mohler, Daniel A. Colón-Ramos. ✉e-mail: daniel.colon-ramos@yale.edu

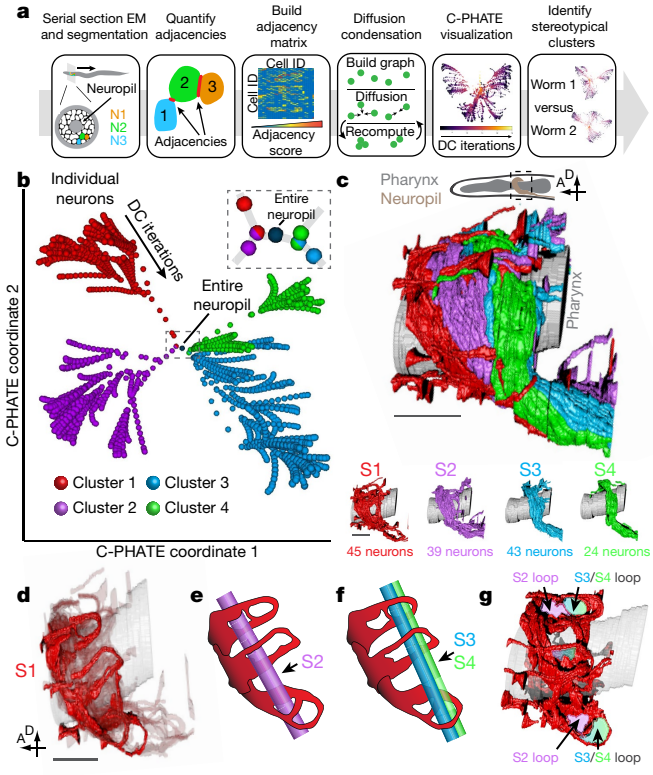

Fig. 1 | Computational detection of a hierarchical tree of neurite organization in the *C. elegans* neuropil. a, Pipeline for analyses of the *C. elegans* neuropil. We used published serial section electron microscopy (EM) data[3] and previously quantified neuron–neuron contacts[18,19] to generate an adjacency matrix, which was analysed by diffusion condensation (DC)[6] and visualized using C-PHATE[28]. L4 and adult worm outputs were quantitatively compared and stereotypical clusters and outliers identified. **b**, C-PHATE plot of diffusion condensation analysis for an L4 worm. Individual neurons are located at the edges of the graph and condense as they move towards the centre. The four clusters identified are individually coloured. C3 and C4 are more closely related than C1 and C2 (Extended Data Fig. 2a–d, Supplementary Videos 1, 2). **c**, Top, volumetric reconstruction of the L4 *C. elegans* neuropil (from electron microscopy serial sections[3]) with the four strata individually coloured. S1–S4 are stacked along the anterior–posterior axis, and S3 is basal to S4. Bottom, representations of individual strata (Extended Data Fig. 1c–h, Supplementary Video 3). **d**, Volumetric reconstruction of S1 perpendicular looping neurons (highlighted in red). A, anterior; D, dorsal. **e**, Schematic of **d** with the trajectory of S2 (in **c**) through specific S1 loops. **f**, As **e**, but with the trajectories of S3 and S4. **g**, The looping structure formed by 32 of the 45 S1 neurons, with loops coloured according to encased strata (in **c**) (Extended Data Fig. 4, Supplementary Videos 4, 5). Scale bars, 5 µm (**c**, **d**).

Supplementary Methods). By iteratively condensing data points closer to their neighbours, DC/C-PHATE outputs dynamically unveil relationships among the data at varying scales of granularity, from cell–cell to circuit–circuit interactions.

Quantitative comparisons of DC/C-PHATE outputs revealed similar—but not identical—clustering patterns between a larva stage 4 (L4) and an adult hermaphrodite nerve ring reconstruction (adjusted Rand index (ARI) of 0.7) (Extended Data Figs. 1a, b, 2f, m, n), which is consistent with previous qualitative descriptions of the stereotyped *C. elegans* nerve ring[3] and with recent analyses of neurite adjacency differences[18,19] (Extended Data Fig. 2e). Our quantitative analyses of the differences in diffusion condensation output between the larva and adult electron microscopy reconstructions also revealed that the differences were underpinned by biologically relevant changes that occur between these developmental stages (Extended Data Fig. 2a–f, q–s, Supplementary Discussion 3). The results of the diffusion condensation analysis of the contact profiles differed from those of the synaptic connectome, and this finding is consistent with structural relationships in the nerve ring being present in the contact profile dataset, but not being represented in the synaptic connectome (Extended Data Fig. 2o, p). However, the examination of clusters throughout the diffusion condensation iterations of contact profiles revealed known cell–cell interactions and behavioural circuits[13,16,17,29–31] (Fig. 1b, c, Extended Data Fig. 3a, b). Together, the contact-based multigranular diffusion condensation outputs enabled understanding of cell–cell interactions within the context of functional circuits, and of functional circuits within the context of higher-order neuropil structures.

Modularity scores, a measure of cluster separation[32], were highest in the diffusion cluster iteration that contained four (L4 dataset) to six (adult dataset) clusters (Fig. 1b, Extended Data Fig. 1a, b, Supplementary Videos 1, 2, Supplementary Discussion 2). Colour-coding the neuron members of the four clusters in the L4 dataset (without unassigned neurons; Supplementary Methods) within the 3D anatomy of the nerve ring revealed that they correspond to distinct, tightly packed layers of neurons within the greater neuropil. These four layers, or strata, stack along the anterior–posterior axis of the worm, encircling the pharynx isthmus. We named these S1, S2, S3 and S4, corresponding to strata 1–4 (Fig. 1c, Extended Data Fig. 1c–h, Supplementary Video 3). Our findings are consistent with those of previous studies that identified an anteroposterior hierarchy of connectivity in the nerve ring[14]. This stratified organization, resolved here at a single-neuron scale, is reminiscent of laminar organizations in the nervous system of *Drosophila*[33] and in the retina and cerebral cortex of vertebrates[34,35].

We noted no clear spaces between the laminar boundaries of the individual strata within the tightly bundled neuropil. However, we identified additional structural features that indicate that these computationally identified strata represent biologically relevant structures. For example, in S1, 32 anterior sensory neurons project axons perpendicular to the neuropil before curling 180° and returning to the anterior limits of the neuropil, where they terminate as synaptic endplates[3,36,37] (Fig. 1d, Extended Data Fig. 4a–d). Notably, these neurite loops circumscribed computationally defined boundaries between S2 and S3/S4. The anterior loops encase around 90% of S2, and the posterior loops encase around 84% of S3 and 100% of S4 (Fig. 1d–g, Extended Data Fig. 4e–k, Supplementary Video 5, Supplementary Table 1). Moreover, the looping neurites form a symmetrical structure along the arc of the neuropil, to both demarcate the individual strata and cage all of the strata within the neuropil (Fig. 1g, Extended Data Fig. 4e–h, Supplementary Video 4).

Sensory information streams in neuropil architecture

To understand the functional anatomy of the nerve ring, we first examined axonal positions of the head sensory neurons within the stratified anatomy of the neuropil. There are two main classes of sensory neuron at the anterior buccal tip of the worm: papillary and amphidial sensilla[36]. Although these two neuron classes are in close proximity, they are distinguishable by distinct dendritic sensory endings, which are thought to reflect distinct sensory modalities[36,37]. Both classes of neuron project axons into the neuropil to transduce sensory information onto the nerve ring[36,37]. We found that the papillary axons project to S1 (Fig. 2a–c), whereas the amphidial axons project to S3 and S4 (Fig. 2a, b, d). No papillary or amphidial axons project to S2. Therefore, these two distinct sensory organs map onto distinct and specific strata, which indicates the functional segregation of sensory information and processing within the layered structure of the neuropil.

We then correlated circuit-based connectomics[3,14] with the strata organization to reveal additional design principles of the functional organization of the neuropil. Within S1, the papillary sensory cells—which are mechanosensory or polymodal—control head withdrawal reflex behaviours[38]. Most neurons in S1 are part of shallow circuits

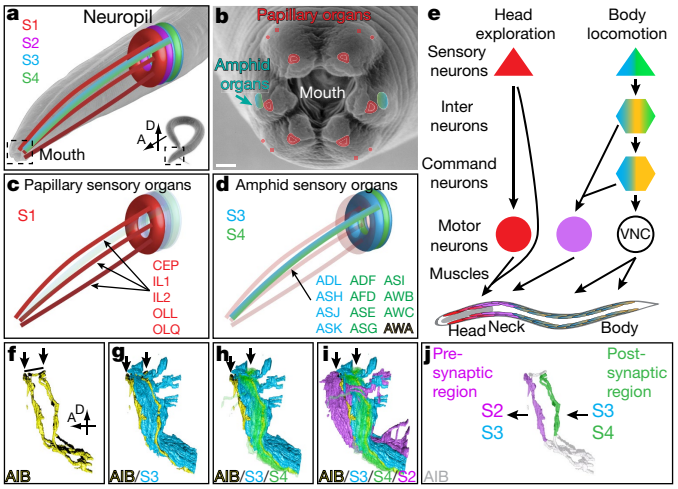

Fig. 2 | Neuropil architecture reflects functional segregation of sensory and motor outputs. a, Representation of head sensilla in the context of the four strata. The representation is projected over a scanning electron microscopy image of *C. elegans* (inset; bottom right), and enlarged to show the head sensilla and strata. Image from WormAtlas, produced by and used with permission of R. Sommer. **b**, Representation of head sensilla, projected over a scanning electron microscopy image of the *C. elegans* mouth (corresponds to dashed box in lower-right of **a**). Image produced by and used with permission of D. Hall. Scale bar, 1 µm. **c**, Schematic of papillary sensillum trajectories from mouth to neuropil. All papillary neurons cluster into S1. Individual neuron classes are listed at the bottom right. **d**, As **c**, but for amphidial sensillum trajectories. BAG head sensory neurons are excluded from the analyses because they are not in a sensillum[3]. **e**, Model of functional segregation of information streams within the neuropil. Papillary sensory information is processed in S1 and innervates head muscles to control head movement. Amphid sensory information is processed in S3 and S4 and links to body muscles (via command interneurons in S3) and neck muscles (via motor neurons in S1 and S2) to control body locomotion[29,38,42]. VNC, ventral nerve cord. Interneurons cross strata to functionally link these modular circuits (Extended Data Fig. 5, and detailed version in Extended Data Fig. 3c). **f**–**i**, Volumetric reconstructions of the unassigned rich-club AIB interneurons[15,20] in the context of nerve ring strata. Arrows indicate the regions of AIB that border strata. The proximal region of the AIB borders S3 and S4 (**g**, **h**), and the distal region borders S2 and S3 (**h**, **i**). The line in **f** indicates the lateral region of AIB that shifts along the anteroposterior axis to change strata. In **h**, S4 is transparent to show AIB bordering S3 and S4 (Supplementary Video 6). **j**, Volumetric rendering of the AIB pair. AIB is a unipolar neuron, with presynaptic specializations enriched in the distal region bordering S2 and S3, and postsynaptic specializations enriched in the proximal region bordering S3 and S4. Arrows indicate synaptic transmission flow (Extended Data Fig. 3g–k). S1, red; S2, purple; S3, blue; S4, green; unassigned, yellow.

formed by papillary sensory cells synapsing onto motor neurons (within S1), or even directly onto head muscles[3,38] (Fig. 2e, Extended Data Fig. 3c). Notably, the S1 circuits retain the symmetry of the papillary sensillum at the interneuron, motor neuron and head neuromuscular synapse level[3,36,37,39]. Topographic maps—the ordered projection of sensory information onto effector systems such as muscles—are a fundamental organizational principle of brain wiring across sensory modalities and organisms[40,41]. We find that S1 displays a topographic map organization, from the primary sensory layer to the motor output representations (Extended Data Fig. 3d–f).

By contrast, amphid sensory axons—which are associated with plastic behaviours[29,42]—innervate S3 and S4. These strata also contain interneurons, but lack motor neurons. Primary and secondary interneurons in S3 and S4 synapse upon motor neurons in S1 and S2 (to innervate head and neck muscles) or upon command interneurons in S3 (that connect to motor neurons which innervate body-wall muscles) (Fig. 2e, Extended Data Fig. 3c). Therefore, information streams from the S3 and S4 amphid sensory axons segregate to control head and neck muscles (through S1 and S2) and body-wall muscles (through S3). These findings concur with cell ablation, behavioural and connectomic studies[16,18,19,43,44], and with anatomical models that show that the *C. elegans* neuropil is functionally regionalized along the anteroposterior axis[3,18,19]. Head-exploration (for example, head-withdrawal reflex) or body-locomotion (for example, chemotaxis) behaviours differentially activate distinct motor strategies in response to sensory information[44], which is consistent with the modular segregation of the sensory information streams that are now observed for the underlying circuits within the strata. Our observations therefore uncover the somatotropic representations of these behavioural strategies in the architecture of the neuropil, revealing functional design principles in the layered structure of the nerve ring, from sensation to motor outputs.

A subset of 'rich-club' interneurons bridge strata

The four neurite strata (S1–S4) account for 151 of the 181 total neurons in the nerve ring (83%). To further understand the structure of the nerve ring, we examined the 30 neurons that clustered differently between the two examined datasets (herein called 'unassigned neurons') (Supplementary Methods). These neurons had one of the following properties: they possessed simple, unbranched processes at boundaries between two adjacent strata (6 neurons); had morphologies that cross strata, such as neurite branches projecting into multiple strata, or single neurites that project across strata (21 neurons); or showed sparse anatomical segmentations (3 neurons) (Extended Data Fig. 5). Notably, 6 unassigned neurons had previously been placed in the 14-member *C. elegans* 'rich-club'[15,20]. Rich-clubs are a conserved organizational feature of neuronal networks in which highly interconnected hub neurons link segregated modules[15]. The *C. elegans* rich-club comprises eight command interneurons (including two from our unassigned set) and six nerve ring interneurons (including four from our unassigned set) (Extended Data Fig. 5g). Additionally, other neurons from our unassigned set—such as RMG and PVR—are hubs of behavioural circuits[43,45,46].

We examined the unassigned neurons in the context of the strata (Extended Data Fig. 5) by focusing on the rich-club interneuron pair of AIBs. The AIB pair was previously shown to morphologically shift between neuronal neighbourhoods[3,47], and we found that the morphology, polarity and position of the AIB neurite are precisely arranged to receive inputs from S3 and S4, and to transduce outputs onto S2 and S3, thereby linking these modular strata. The proximal AIB neurite region lies on the S3/S4 border, while a perpendicular shift of precisely the width of S3 positions the distal region at the S2/S3 border (Fig. 2f–i, Supplementary Video 6). To examine the output performance of the diffusion condensation algorithm, we digitally dissected the AIB neurite into distal and proximal regions and observed—as expected—that the proximal region of AIB specifically clustered with its neighbouring S4, while the distal region clustered with its neighbouring S2 (Extended Data Fig. 3i–k). The synapses of AIB are similarly partitioned: postsynaptic specializations are primarily in the proximal region in the amphid sensory-rich strata (S3 and S4), whereas presynaptic specializations are localized to the distal region in the motor neuron-rich stratum (S2) (Fig. 2j, Extended Data Fig. 3g, h). This architecture is consistent with the role of AIB in processing amphid-derived sensory stimuli to mediate locomotory strategies[44,48]. Another rich-club interneuron pair, AVE, has a similar morphology to AIB: its proximal neurite region borders S2 and S3, and its distal region borders S1 and S2 (Extended Data Fig. 5a–d, Supplementary Video 7). Neurites of other rich-club neurons (RIB and RIA) and 'unassigned' neurons (AIZ) similarly shift across the strata (Extended Data Fig. 5a–d, g–u).

Our analyses reveal design principles of the *C. elegans* neuropil at varying degrees of granularity—from single rich-club neuron morphologies that functionally bridge different strata, to layered strata that

segregate sensory–motor information onto somatotropic representations. These design principles are important organizational units in neuroscience: rich-clubs in the context of brain networks[15,20], laminar organization in the context of brain structures[33,34], and topographical maps in the context of vertebrate sensory systems[40,41].

Layered strata correlate with neuronal cell migrations

To examine the developmental sequence that leads to assembly of the layered nerve ring, we used an integrated platform for long-term, four-dimensional, in vivo imaging of embryos. The platform achieves isotropic resolution[7,8,49,50], systematic lineage-tracing[9,10] and rendering of cell movements and neuronal outgrowth (represented in the 4D WormGUIDES atlas[51]; https://wormguides.org) (Fig. 3a). The embryonic atlas was systematically examined for birth order, soma positions and lineage identity for all neurons within the strata (Fig. 3b, c, Extended Data Fig. 6). Despite the previous hypothesis that lineage-dependent neuronal soma positions might influence neurite outgrowth into neighbourhoods[47], we could not detect any relationships between ancestry or newborn-cell position and the final neurite position within the neuropil strata (Fig. 3b, Extended Data Fig. 6).

Quantification of the positions of individual neurons (belonging to specific strata) in the context of the spatio-temporal dynamics of embryo morphogenesis revealed stereotypical coordinated cell movements that segregated and co-located the cell bodies of future S1 stratum. Cell bodies of neurons that later project onto S1 migrated and co-located to the anterior part of the embryo head (anterior to the future neuropil position), whereas cell bodies of neurons that later project onto S2–S4 migrated to the posterior part of the head (Fig. 3b–d, Extended Data Fig. 7, Supplementary Video 8). For all strata, embryonic soma positions persist until adulthood, and for the future S1 stratum, relate to the cellular morphologies of posteriorly projecting axonal structures within the anterior stratum of the nerve ring[3,36,37].

In vertebrate embryogenesis, migration of waves of neurons helps to organize the layered architecture of the retina and the brain cortex[52]. We found that co-segregation of S1 somas in early embryogenesis might serve as an initial organizing principle to define the axes for anteroposterior layering, and later functional segregation of the sensory–motor architecture within the neuropil.

Hierarchical development of the layered neuropil

Previous genetic studies that examined formation of the nerve ring demonstrated roles for glia and centrally located pioneering neurons in its development[21–24]. To build on these findings, we examined neurite outgrowth dynamics during embryonic neuropil formation (Extended Data Fig. 8a–f, Supplementary Video 9). At approximately 390–400 minutes post fertilization (mpf) we observed cells sending projections into the area of the future nerve ring (Fig. 3e, g). Through the simultaneous use of *mCherry::histone* (to trace the lineage of these cells) and ubiquitous membrane-tethered GFP (to observe outgrowth), we identified six of these cells as three bilateral pairs of neurons—SIAD, SIBV and SMDD—consistent with pioneering neurons previously identified[21,22] (the four-letter name represents a left and right bilateral neuron pair; that is, SIADL and SIADR, Fig. 3f, h). Additional neurons were observed sending neurite projections alongside these pioneers, but dense ubiquitous membrane labelling prevented us from identifying them by lineaging. To confirm the identities of the three lineaged neuron pairs and identify the additional early-outgrowth neurons, we co-labelled embryos with ubiquitous *membrane::gfp* and a cytoplasmic *lim-4p::mCherry* reporter gene (lineaged[51] to express in SIAD, SIBV and SMDD (Extended Data Fig. 8g–j) and in RIV, SAAV, SIAV, SIBD and SMDV)). We found that all eight neuron pairs extend neurites into the future neuropil as a tight bundle at 390–400 mpf (Fig. 3i–k, Supplementary Video 10). To further analyse outgrowth timing, we

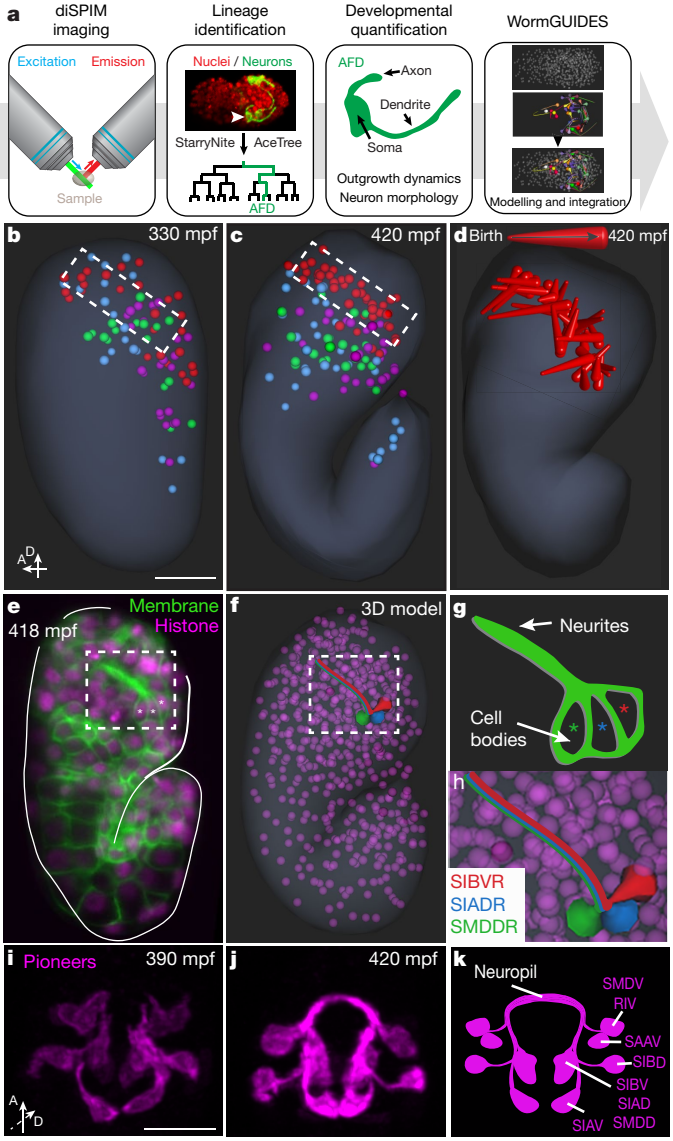

Fig. 3 | Developmental processes guide layered neuropil assembly. **a**, Analyses pipeline for *C. elegans* embryonic neurodevelopment. Embryonic neurodevelopment was imaged by dual-view inverted selective plane illumination microscopy (diSPIM)[7,8,49,50] and cell lineages were determined using StarryNite[9] and AceTree[10]. Neuronal outgrowth and morphology were quantified, and information incorporated into the WormGUIDES atlas[51]. **b**, WormGUIDES atlas representation of all embryonic neuronal soma positions at 330 mpf. Somas are coloured as in Fig. 1c to show their eventual neurite strata assignment. **c**, As **b**, but at 420 mpf. The dashed boxes in **b** and **c** represent the final anterior position of the migrating S1 neurons (Extended Data Fig. 7a–h, Supplementary Video 8). **d**, Three-dimensional depth trajectories of S1-cell movements between neuronal cell birth and 420 mpf. **e**, Comma stage embryo labelled with ubiquitous *nhr-2p::membrane::gfp* and *mCherry::histone*. Asterisks denote the three lineaged cells. The image is a single *z*-slice from a diSPIM arm (three embryos were lineaged; Extended Data Fig. 8a–f, Supplementary Video 9). **f**, WormGUIDES atlas 3D model of the three cells observed in **e**. **g**, Cartoon of the inset of the three cells observed in **e**; asterisks denote somas of lineaged cells. **h**, Enlargement of the inset in **f**, with early outgrowing cells identified via lineaging, coloured to highlight cellular locations. **i**–**k**, Time-lapse of the outgrowth dynamics of pioneer neurons and schematic (labelled with *lim-4p::membrane-tethered::gfp*; *lim-4p* embryonic expression was previously lineaged to the eight neuron pairs listed in **k**[51]). Images are deconvolved diSPIM maximum intensity projections ($n = 16$ embryos) (Extended Data Fig. 8g–r, Supplementary Video 10). Scale bar, 10 µm (**b**–**f**, **i**, **j**).

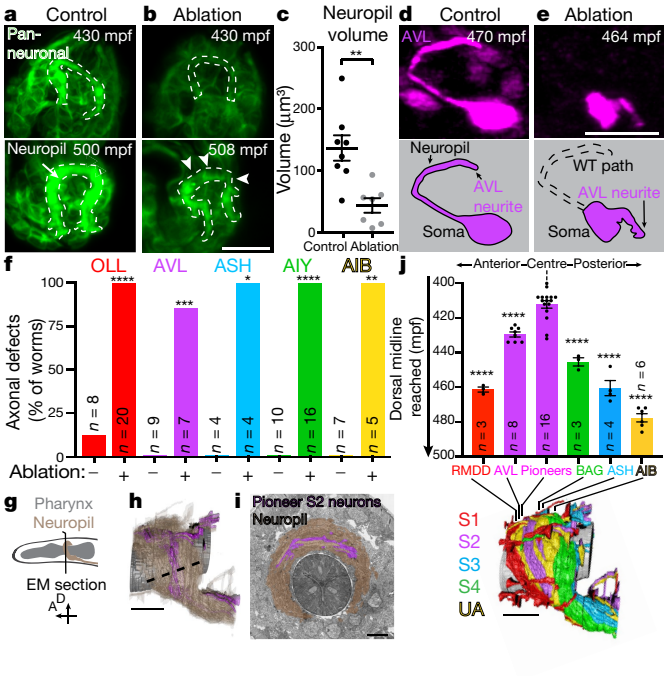

Fig. 4 | Temporal progression of outgrowth guided by pioneer neurons results in inside-out neuropil development. a, **b**, Neuropil development in control (**a**) or pioneer-ablated (**b**) embryos monitored by pan-neuronal *ceh-48p::membrane-tethered::gfp*. Dashed lines represent the control neuropil ($n = 8$ embryos; ablation, $n = 7$ embryos). Maximum intensity projections from one diSPIM arm (Supplementary Video 12). **c**, Quantification of neuropil volume for control or pioneer-ablated worms. Data are mean ± s.e.m., with individual data points shown (control, $n = 8$; ablation, $n = 7$). $^{**}P = 0.0023$ by unpaired two-tailed Student's *t*-test comparing control and ablation (Extended Data Fig. 8y, z). **d**, **e**, AVL development in control (**d**) or pioneer-ablated (**e**) embryos monitored using an AVL-specific promoter (*lim-6p::gfp*). The dashed line depicts normal AVL outgrowth (control, $n = 9$ embryos; ablation, $n = 7$ embryos). Deconvolved diSPIM maximum intensity projections are shown (Supplementary Video 13). **f**, Quantification of neurite outgrowth for the indicated neurons from each stratum in control and pioneer-ablated worms. The values of *n* represent the number of embryos (AVL, ASH, AIB) or L1 worms (OLL, AIY) scored. $^{*}P < 0.05$, $^{**}P < 0.01$, $^{***}P < 0.001$, $^{****}P < 0.0001$ by two-sided Fisher's exact test comparing control and ablation for each neuron (see Supplementary Methods for exact *P* values) (Extended Data Fig. 9). **g**, Schematic of worm head; the line marks the position of the electron microscopy cross-section shown in **h**, **i**. **h**, Volumetric reconstruction of the *C. elegans* L4 neuropil. Centrally located S2 pioneer neurons, purple; neuropil, brown; pharynx, grey. The dashed line indicates the width of the neuropil. **i**, Segmented serial section electron microscopy image[3], coloured as in **h** (section corresponds to the L4 worm *z*-slice 54). S2 pioneers are centrally located in the neuropil. Electron microscopy image used with permission from D. Hall. Scale bar, 2.5 µm. **j**, Top, analysis of dorsal midline outgrowth for neurons from each stratum. Bottom, a volumetric neuropil reconstruction with the terminal location, along the dorsal midline, of the examined neurons. The values of *n* represent the number of embryos scored. Data are mean ± s.e.m. $^{****}P < 0.0001$ by one-way ANOVA with Tukey's post hoc analysis comparing pioneer neurons and each representative neuron. For statistical analysis of all pairwise comparisons, see Supplementary Methods (Extended Data Fig. 10a–j). The colours in **d**–**f**, **j** indicate the strata to which the neurons are assigned. Scale bars, 10 µm (**a**, **b**, **d**, **e**); 5 µm (**h**, **j**).

co-labelled embryos with a *pan-neuronal::membrane::gfp* marker and the *lim-4p::mCherry* marker, and observed that these eight neuron pairs displayed the earliest outgrowth events for the neuropil (Extended Data Fig. 8k–r, Supplementary Videos 10, 11).

All eight neuron pairs belong to a neuronal group that is centrally located in S2 (Fig. 4g–i). To examine the pioneering roles of these neurons in strata formation, we adapted an in vivo split-caspase ablation system[53] that ablated these neuron pairs during embryonic neurodevelopment (Extended Data Fig. 8s–x). We then quantified neuropil formation via a *pan-neuronal::membrane::gfp* (Supplementary Video 12). Ablation of the putative eight pioneering neuron pairs resulted in larval stage 1 (L1) arrested worms, and aberrant embryonic neuropils (mean embryonic control volume, 136.6 µm^3; compared with ablated neuropil volume, 43.6 µm^3) (Fig. 4a–c, Extended Data Fig. 8y, z). Systematic examination of a representative neuron from each stratum (using cell-specific promoters) revealed that ablation of putative pioneer neurons affected the outgrowth of all examined neurons (Fig. 4d–f, Extended Data Fig. 9). In all cases, neurites paused indefinitely near the positions of the ablated pioneer somas. The embryonic organization of neuropil strata therefore seems to be pioneered by a subset of centrally located S2 neurons.

To understand the role of the pioneer neurons in strata formation, we analysed synchronized recordings of embryonic neurite outgrowth. An ordered sequence of outgrowth events emerged, in which the timing of neurite arrival at the dorsal midline of the neuropil correlated with the axial proximity of the examined neurites to the centrally located pioneer neurites (Fig. 4j, Extended Data Fig. 10a–j′, Supplementary Videos 13–15). Our findings extend observations on the hierarchical formation of the neuropil[22], placing the ordered sequence of events within the context of the strata.

Temporal correlation was specific to arrival at the dorsal midline, but not to initiation of outgrowth from the soma. Notably, the S4 neuron AWC was observed initiating outgrowth at 390–400 mpf—a similar time to the pioneering neurons (Fig. 3i, Extended Data Fig. 10k). However, instead of entering the nerve ring with the pioneer neurons, AWC neurites paused for 20.6 min (s.e.m. ±2.8 min) near the pioneering SAAV somas before entering the nerve ring (Fig. 3i, j, Extended Data Fig. 10k–s). This pausing point corresponds to the stalling point seen in our pioneer neuron ablation studies (Extended Data Fig. 9c, h, v, y). Therefore, although the initial outgrowth events for some neurons occur simultaneously, neurites extend to—and pause at—specific nerve ring entry sites.

The temporal sequence of neurite entries into the nerve ring continues throughout embryogenesis. For example, both the neurites of strata-crossing AIBs and the looping S1 neurons outgrow after the neuropil has formed a ring structure (at around 420 mpf) and after all the representative neurons of the four strata have reach the dorsal midline (around 460 mpf)[50] (Figs. 3i, j, 4j, Extended Data Fig. 10f–j′, t, u″). Our observations suggest an inside-out developmental model in which the strata are assembled through the timed entry of their components: a pioneering bundle founds centrally located S2; then other S2 neurons enter, followed by peripherally located S1 (anterior) and S3 and S4 (posterior) neurons; followed by the outgrowth of neurons that link the strata, such as the S1 looping neurons or the neurons that cross strata (such as AIB).

Lamination is a conserved principle of organization within brains[33,34]. Segregation of functional circuits into layers underpins information processing in sensory systems and higher order structures[35]. In this study we resolve these conserved features of brain organization at a single-cell level and in the context of the nerve ring neuropil, thereby linking fundamental design principles of neuropil organization with the developmental processes that underpin their assembly. Our findings provide a blueprint for the synergistic integration of structural connectomic analyses and developmental approaches to systematically understand neuropil organization and development within brains.

Online content

Any methods, additional references, Nature Research reporting summaries, source data, extended data, supplementary information, acknowledgements, peer review information; details of author contributions and competing interests; and statements of data and code availability are available at https://doi.org/10.1038/s41586-020-03169-5.

1. Maynard, D. M. Organization of neuropil. *Am. Zool.* **2**, 79–96 (1962).
2. Schürmann, F. W. Fine structure of synaptic sites and circuits in mushroom bodies of insect brains. *Arthropod Struct. Dev.* **45**, 399–421 (2016).
3. White, J. G., Southgate, E., Thomson, J. N. & Brenner, S. The structure of the nervous system of the nematode *Caenorhabditis elegans*. *Phil. Trans. R. Soc. Lond. B* **314**, 1–340 (1986).
4. Soiza-Reilly, M. & Commons, K. G. Unraveling the architecture of the dorsal raphe synaptic neuropil using high-resolution neuroanatomy. *Front. Neural Circuits* **8**, 105 (2014).
5. Zheng, Z. et al. A complete electron microscopy volume of the brain of adult *Drosophila melanogaster*. *Cell* **174**, 730–743.e22 (2018).
6. Brugnone, N. et al. Coarse graining of data via inhomogeneous diffusion condensation. In *2019 IEEE International Conference on Big Data* 2624–2633 (IEEE, 2019).
7. Kumar, A. et al. Dual-view plane illumination microscopy for rapid and spatially isotropic imaging. *Nat. Protoc.* **9**, 2555–2573 (2014).
8. Wu, Y. et al. Spatially isotropic four-dimensional imaging with dual-view plane illumination microscopy. *Nat. Biotechnol.* **31**, 1032–1038 (2013).
9. Bao, Z. et al. Automated cell lineage tracing in *Caenorhabditis elegans*. *Proc. Natl Acad. Sci. USA* **103**, 2707–2712 (2006).
10. Boyle, T. J., Bao, Z., Murray, J. I., Araya, C. L. & Waterston, R. H. AceTree: a tool for visual analysis of *Caenorhabditis elegans* embryogenesis. *BMC Bioinformatics* **7**, 275 (2006).
11. Sulston, J. E., Schierenberg, E., White, J. G. & Thomson, J. N. The embryonic-cell lineage of the nematode *Caenorhabditis elegans*. *Dev. Biol.* **100**, 64–119 (1983).
12. Azulay, A., Itskovits, E. & Zaslaver, A. The *C. elegans* connectome consists of homogenous circuits with defined functional roles. *PLoS Comput. Biol.* **12**, e1005021 (2016).
13. Chatterjee, N. & Sinha, S. Understanding the mind of a worm: hierarchical network structure underlying nervous system function in *C. elegans*. *Prog. Brain Res.* **168**, 145–153 (2008).
14. Cook, S. J. et al. Whole-animal connectomes of both *Caenorhabditis elegans* sexes. *Nature* **571**, 63–71 (2019).
15. Towlson, E. K., Vertes, P. E., Ahnert, S. E., Schafer, W. R. & Bullmore, E. T. The rich club of the *C. elegans* neuronal connectome. *J. Neurosci.* **33**, 6380–6387 (2013).
16. Varshney, L. R., Chen, B. L., Paniagua, E., Hall, D. H. & Chklovskii, D. B. Structural properties of the *Caenorhabditis elegans* neuronal network. *PLoS Comput. Biol.* **7**, e1001066 (2011).
17. Yan, G. et al. Network control principles predict neuron function in the *Caenorhabditis elegans* connectome. *Nature* **550**, 519–523 (2017).
18. Brittin, C. A., Cook, S. J., Hall, D. H., Emmons, S. W. & Cohen, N. Volumetric reconstruction of main *Caenorhabditis elegans* neuropil at two different time points. Preprint at https://doi.org/10.1101/485771 (2018).
19. Brittin, C. A., Cook, S. J., Hall, D. H., Emmons, S. W. & Cohen, N. A multi-scale brain map derived from whole-brain volumetric reconstructions. *Nature* https://doi.org/10.1038/s41586-021-03284-x (2021).
20. Sabrin, K. M., Wei, Y., van den Heuvel, M. P. & Dovrolis, C. The hourglass organization of the *Caenorhabditis elegans* connectome. *PLoS Comput. Biol.* **16**, e1007526 (2020).
21. Kennerdell, J. R., Fetter, R. D. & Bargmann, C. I. Wnt-Ror signaling to SIA and SIB neurons directs anterior axon guidance and nerve ring placement in *C. elegans*. *Development* **136**, 3801–3810 (2009).
22. Rapti, G., Li, C., Shan, A., Lu, Y. & Shaham, S. Glia initiate brain assembly through noncanonical Chimaerin–Furin axon guidance in *C. elegans*. *Nat. Neurosci.* **20**, 1350–1360 (2017).
23. Wadsworth, W. G., Bhatt, H. & Hedgecock, E. M. Neuroglia and pioneer neurons express UNC-6 to provide global and local netrin cues for guiding migrations in *C. elegans*. *Neuron* **16**, 35–46 (1996).
24. Yoshimura, S., Murray, J. I., Lu, Y., Waterston, R. H. & Shaham, S. *mls-2* and *vab-3* control glia development, *hlh-17*/Olig expression and glia-dependent neurite extension in *C. elegans*. *Development* **135**, 2263–2275 (2008).
25. Blondel, V. D., Guillaume, J. L., Lambiotte, R. & Lefebvre, E. Fast unfolding of communities in large networks. *J. Stat. Mech. Theory Exp.* P10008, (2008).
26. Dasgupta, A., Hopcroft, J., Kannan, R. & Mitra, P. Spectral clustering by recursive partitioning. *Lect. Notes Comput. Sci.* **4168**, 256–267 (2006).
27. Kaufman, L. & Rousseeuw, P. J. *Finding Groups in Data: An Introduction to Cluster Analysis* (Wiley, 2005).
28. Moon, K. R. et al. Visualizing structure and transitions in high-dimensional biological data. *Nat. Biotechnol.* **37**, 1482–1492 (2019).
29. Bargmann, C. I. Chemosensation in *C. elegans*. In *WormBook* (ed. The *C. elegans* Research Community) https://doi.org/10.1895/wormbook.1.123.1 (2006).
30. Goodman, M. B. Mechanosensation. In *WormBook* (ed. The *C. elegans* Research Community) https://doi.org/10.1895/wormbook.1.62.1 (2006).
31. Goodman, M. B. & Sengupta, P. How *Caenorhabditis elegans* senses mechanical stress, temperature, and other physical stimuli. *Genetics* **212**, 25–51 (2019).
32. Newman, M. E. Modularity and community structure in networks. *Proc. Natl Acad. Sci. USA* **103**, 8577–8582 (2006).
33. Millard, S. S. & Pecot, M. Y. Strategies for assembling columns and layers in the *Drosophila* visual system. *Neural Dev.* **13**, 11 (2018).
34. Sanes, J. R. & Zipursky, S. L. Design principles of insect and vertebrate visual systems. *Neuron* **66**, 15–36 (2010).
35. Baier, H. Synaptic laminae in the visual system: molecular mechanisms forming layers of perception. *Annu. Rev. Cell Dev. Biol.* **29**, 385–416 (2013).
36. Ware, R. W., Clark, D., Crossland, K. & Russell, R. L. Nerve ring of nematode *Caenorhabditis elegans*: sensory input and motor output. *J. Comp. Neurol.* **162**, 71–110 (1975).
37. Ward, S., Thomson, N., White, J. G. & Brenner, S. Electron microscopical reconstruction of the anterior sensory anatomy of the nematode *Caenorhabditis elegans*. *J. Comp. Neurol.* **160**, 313–337 (1975).
38. Riddle, D. L., Blumenthal, T., Meyer, B. J. & Priess, J. R. (eds) *C. elegans II* 2nd edn (Cold Spring Harbor Lab. Press, 1997).
39. White, J. Clues to basis of exploratory behaviour of the *C. elegans* snout from head somatotropy. *Phil. Trans. R. Soc. Lond. B* **373**, (2018).
40. Groh, J. M. *Making Space: How The Brain Knows Where Things Are* (Harvard Univ. Press, 2014).
41. Kaas, J. H. Topographic maps are fundamental to sensory processing. *Brain Res. Bull.* **44**, 107–112 (1997).
42. Sasakura, H. & Mori, I. Behavioral plasticity, learning, and memory in *C. elegans*. *Curr. Opin. Neurobiol.* **23**, 92–99 (2013).
43. Chalfie, M. et al. The neural circuit for touch sensitivity in *Caenorhabditis elegans*. *J. Neurosci.* **5**, 956–964 (1985).
44. Gray, J. M., Hill, J. J. & Bargmann, C. I. A circuit for navigation in *Caenorhabditis elegans*. *Proc. Natl Acad. Sci. USA* **102**, 3184–3191 (2005).
45. Lockery, S. R. Neuroscience: A social hub for worms. *Nature* **458**, 1124–1125 (2009).
46. Macosko, E. Z. et al. A hub-and-spoke circuit drives pheromone attraction and social behaviour in *C. elegans*. *Nature* **458**, 1171–1175 (2009).
47. White, J. G., Southgate, E., Thomson, J. N. & Brenner, S. Factors that determine connectivity in the nervous system of *Caenorhabditis elegans*. *Cold Spring Harb. Symp. Quant. Biol.* **48**, 633–640 (1983).
48. Wakabayashi, T., Kitagawa, I. & Shingai, R. Neurons regulating the duration of forward locomotion in *Caenorhabditis elegans*. *Neurosci. Res.* **50**, 103–111 (2004).
49. Duncan, L. H. et al. Isotropic light-sheet microscopy and automated cell lineage analyses to catalogue *Caenorhabditis elegans* embryogenesis with subcellular resolution. *J. Vis. Exp.* (2019).
50. Guo, M. et al. Rapid image deconvolution and multiview fusion for optical microscopy. *Nat. Biotechnol.* (2020).
51. Santella, A. et al. WormGUIDES: an interactive single cell developmental atlas and tool for collaborative multidimensional data exploration. *BMC Bioinformatics* **16**, 189 (2015).
52. Ayala, R., Shu, T. & Tsai, L. H. Trekking across the brain: the journey of neuronal migration. *Cell* **128**, 29–43 (2007).
53. Chelur, D. S. & Chalfie, M. Targeted cell killing by reconstituted caspases. *Proc. Natl Acad. Sci. USA* **104**, 2283–2288 (2007).

Reporting summary

Further information on research design is available in the Nature Research Reporting Summary linked to this paper.

Data availability

The datasets generated during and/or analysed during the study are available from the corresponding author upon request. To facilitate exploration of the placement of neurites in the C-PHATE diagrams, we have generated a 3D interactive version of the C-PHATE plots. Plots can be downloaded, and neurite condensation and position can be examined. These 3D interactive versions enable identification of any neuron within the C-PHATE plot and provide the iteration number and total neurons found within any cluster. See Supplementary Discussion 2 for instructions on how to access the data. Source data are provided with this paper.

Code availability

Electron micrograph segmentation adjacency analysis code is available in ref. [18]. Diffusion condensation analysis code[6] is available at https://github.com/agonopol/worm_brain. C-PHATE visualization code is available to download at http://dccphate.wormguides.org/CPHATE_pythonCode.zip.

54. Brandes, U. et al. On modularity clustering. *IEEE Trans. Knowl. Data Eng.* **20**, 172–188 (2008).
55. Wicks, S. R. & Rankin, C. H. Integration of mechanosensory stimuli in *Caenorhabditis elegans*. *J. Neurosci.* **15**, 2434–2444 (1995).
56. Walthall, W. W. & Chalfie, M. Cell–cell interactions in the guidance of late-developing neurons in *Caenorhabditis elegans*. *Science* **239**, 643–645 (1988).
57. Kindt, K. S. et al. *Caenorhabditis elegans* TRPA-1 functions in mechanosensation. *Nat. Neurosci.* **10**, 568–577 (2007).
58. Insley, P. & Shaham, S. Automated *C. elegans* embryo alignments reveal brain neuropil position invariance despite lax cell body placement. *PLoS ONE* **13**, e0194861 (2018).
59. Shah, P. K. et al. An in toto approach to dissecting cellular interactions in complex tissues. *Dev. Cell* **43**, 530–540.e4 (2017).
60. Lu, N., Yu, X., He, X. & Zhou, Z. Detecting apoptotic cells and monitoring their clearance in the nematode *Caenorhabditis elegans*. *Methods Mol. Biol.* **559**, 357–370 (2009).

Acknowledgements We thank S. Emmons, S. Cook and C. Brittin for sharing the segmented electron microscopy datasets and adjacency analysis code, and for comments on this work; O. Hobert for sharing the *ceh-48p* promoter and for advice; Z. Zhou for sharing a 2xFYVE-containing plasmid; J. White for transferring the electron microscopy data archive from MCR/LMB to the laboratory of D. Hall for long-term curation and display on the WormImage website (website supported by NIH grant no. OD010943 to D.H.); D. Hall for use of the young adult scanning electron microscopy images, for advice, and for help with electron microscopy images; R. Sommer for use of an electron microscopy image; H. Eden for comments on the manuscript; and members of the D.A.C-R. laboratory for comments during manuscript preparation. We thank the Caenorhabditis Genetic Center (funded by National Institutes of Health (NIH) Office of Research Infrastructure Programs P40 OD010440) for *C. elegans* strains; the Research Center for Minority Institutions program; the Marine Biological Laboratories (MBL); and the Instituto de Neurobiología de la Universidad de Puerto Rico for providing meeting and brainstorming platforms. H.S. and D.A.C-R. acknowledge the Whitman and Fellows program at MBL for providing funding and space for discussions valuable to this work. H.S. and D.A.C-R. are MBL Fellows. Research in the D.A.C.-R., W.A.M. and Z.B. laboratories was supported by NIH grant no. R24-OD016474. M.W.M. was supported by NIH grant no. F32-NS098616. Research in the H.S. laboratory was further supported by the intramural research program of the National Institute of Biomedical Imaging and Bioengineering (NIBIB), NIH. Research in the Z.B. laboratory was further supported by an NIH center grant to MSKCC (P30CA008748). Research in the D.A.C.-R. laboratory was further supported by NIH grant nos R01NS076558 and DP1NS111778 and by an HHMI Scholar Award.

Author contributions M.W.M., K.M.B., M.K., A.G., L.H.D., A.S., K.R.M., G.W., S.K., Z.B., H.S., W.A.M. and D.A.C.-R. designed experiments; M.W.M., K.M.B. and L.H.D. performed biological experiments; M.W.M., K.M.B., M.K., A.G., A.S., G.W. and W.A.M. performed computational experiments; M.W.M., L.H.D. and T.S. generated reagents; M.W.M., T.S., L.S., M.G., A.S., A.K., Y.W. and W.A.M. built instrumentation and analysis software; M.W.M., K.M.B., L.H.D., A.S., R.C., Z.B. and W.A.M. contributed lineaging data and expertise; M.W.M., W.A.M. and D.A.C.-R. prepared the manuscript with assistance from all authors; S.K., Z.B., H.S., W.A.M. and D.A.C.-R. supervised the research; and D.A.C.-R. directed the research.

Competing interests The authors declare no competing interests.

Additional information
Supplementary information The online version contains supplementary material available at https://doi.org/10.1038/s41586-020-03169-5.
Correspondence and requests for materials should be addressed to D.A.C.-R.
Peer review information *Nature* thanks John White and the other, anonymous, reviewer(s) for their contribution to the peer review of this work. Peer reviewer reports are available.
Reprints and permissions information is available at http://www.nature.com/reprints.

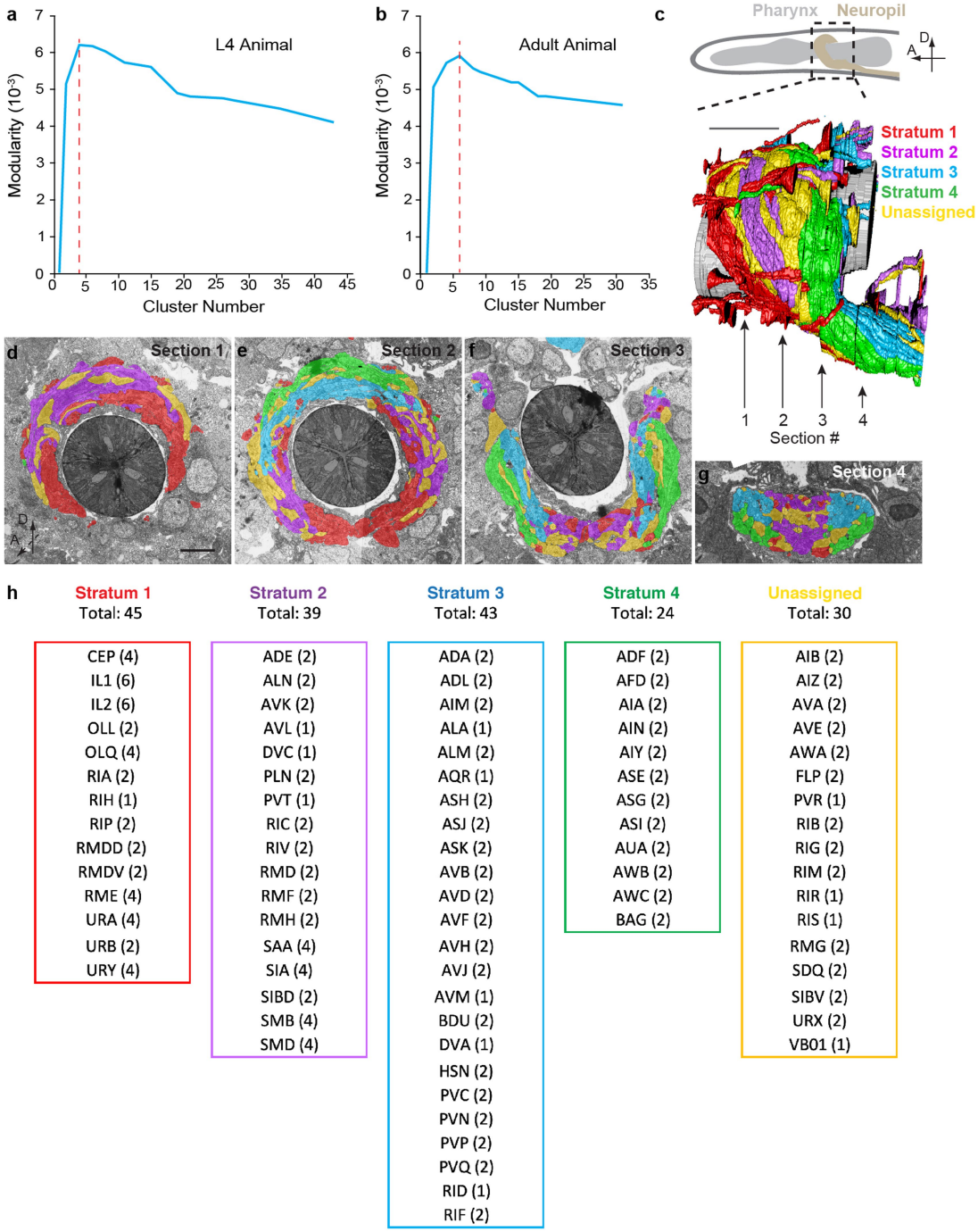

Extended Data Fig. 1 | Diffusion condensation analyses of the nerve ring neuropil. a, **b**, Quantification of network modularity[32,54] for diffusion condensation (DC) analysis of L4 (**a**) and adult (**b**) animals. DC iteratively groups neurons on the basis of quantitative similarities of each neuron's contact profile, unveiling data relationships at varying scales of granularity (Fig. 1b). We calculated network modularity for each iteration. The highest modularity score was for the iteration with four clusters (in the L4 stage animal) and 6 clusters (in the adult animal). Comparisons revealed that for the adult animal, there were four large clusters similar to the L4 stage animal, and two smaller ones (Supplementary Methods; Extended Data Fig. 2a–d). Some of these neurons from the two smaller clusters in the adult also clustered in the L4 animal, but in an earlier iteration (Extended Data Fig. 2m, n). The iterations with the highest modularity scores were then used for subsequent strata analyses in the manuscript (Supplementary Methods), but we emphasize that other iterations reveal other valuable data relationships at varying scale of granularity, including cell–cell and circuit– circuit interactions (Extended Data Fig. 3a, b). **c**, Volumetric reconstruction of the L4 stage *C. elegans* neuropil (from EM serial sections[3]) with the 4 strata and unassigned neurons individually coloured. Above, schematic of worm head with nerve ring neuropil (dashed box). Location of EM sections displayed in **d**–**g** shown below (arrows and corresponding section numbering). Scale bar, 5 µm. **d**–**g**, Segmented serial section electron micrographs[3], neurons coloured as in **c**. Original EM slices 41, 92, 152, 206 shown in **d**–**g**, respectively. Electron microscopy images used with permission from D. Hall. Scale bar (2.5 µm, in **d**) applies to **d**–**g**. **h**, Listing of neuronal classes in the 4 strata, and the 'unassigned' group. The number to the right of each neuron represents total neurons for each class, for all 181 neurons in the nerve ring neuropil.

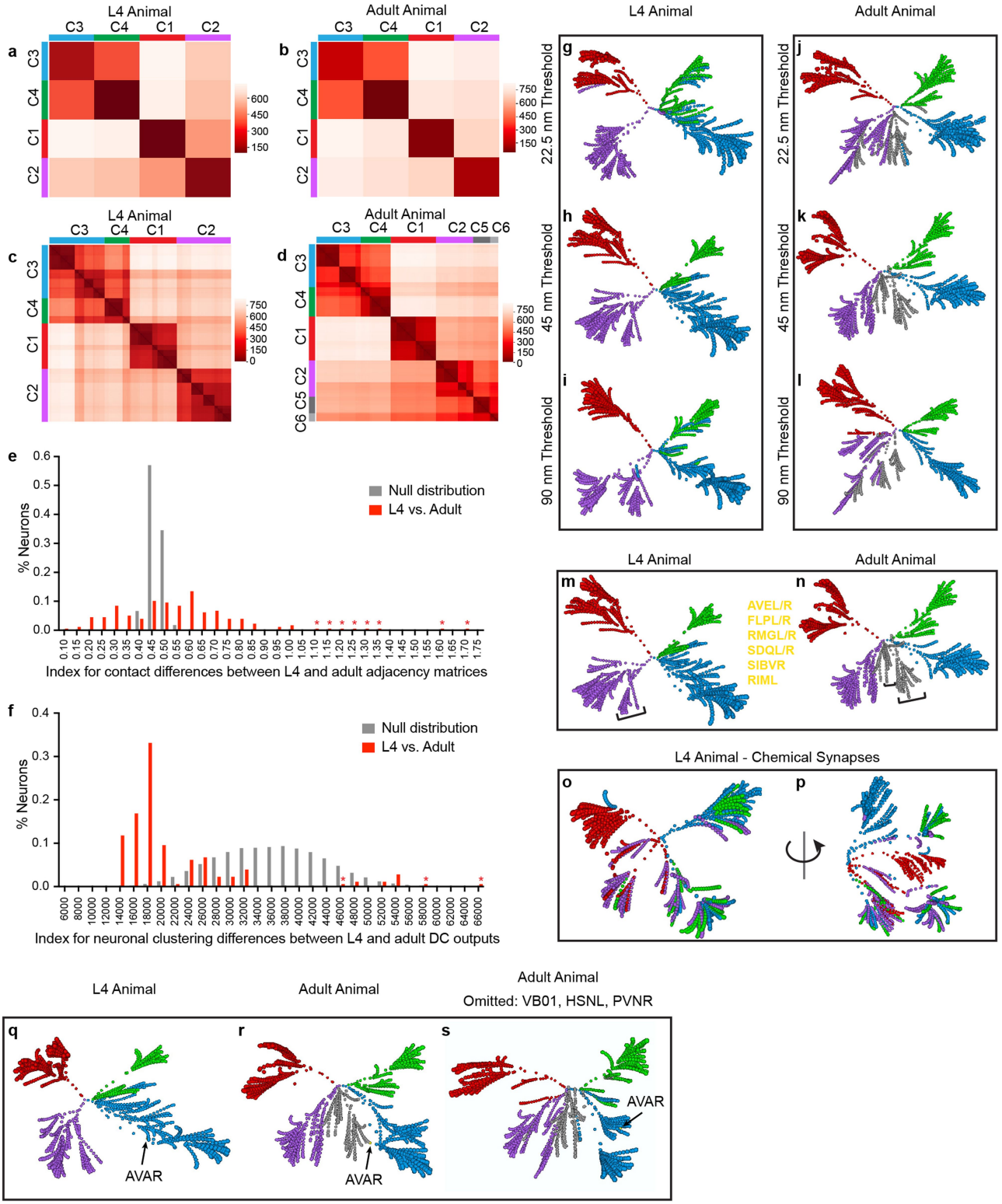

Extended Data Fig. 2 | See next page for caption.

Extended Data Fig. 2 | Analyses of the L4 and adult contact adjacency matrices, DC outputs, and C-PHATE plots. a, **b**, Heat map of scaled neuron distances within the DC nested hierarchy outputs for the L4 (**a**) and adult (**b**) animal. Values were calculated by measuring all distances between neurons from one cluster to another cluster and then averaged (Supplementary Methods). This was done for the clusters at the iteration with the highest modularity score (see Fig. 1b and Extended Data Fig. 1a, b). The two smaller clusters from the adult were excluded. Colouring scale displayed to the right of the heat map. Darker colours indicate smaller average distance. Note how C3 is closer to C4 and C1 is closer to C2 in distance. **c**, **d**, As **a**, **b**, except scaled distance values were calculated by measuring the distances between every neuron within the DC output. Two additional clusters in the adult are coloured grey. Note varying scales of granularity in neuronal relationships that constitute the major clusters, and, similar to the C-PHATE plots, circuits such as thermotaxis and body mechanosensation can be found in the more granular areas (Extended Data Fig. 3a, b). **e**, Histogram of the distribution of contact profile differences for each neuron between the L4 and adult contact adjacency matrices. In brief, we calculated an index of difference (Supplementary Methods section (in Supplementary Information) entitled 'Contact adjacency data analysis') for each neuron, comparing the contact profiles of the adult and L4 animals. We also generated 2,004 random adjacency matrices to simulate distributions of random contact profile differences. We determined that the contact profiles of 49/178 neurons (28%) were significantly more similar than random ($P < 0.05$), whereas the contact profiles of 96/178 neurons (54%) were significantly more different ($P < 0.05$; by unpaired two-tailed Student's *t*-test between L4 vs. Adult and null distribution; degrees of freedom (df) = 178,532, no adjustments were made for multiple comparisons; Supplementary Methods). Therefore, there are a substantial portion of neurons that have statistically different contact profiles between L4 and adult. Additionally, we calculated the Jaccard distance and found that the average neuron's contact partner list was 37.6% different between the L4 and adult animal, consistent with previous analysis[18]. As further discussed in Supplementary Discussion 3, we think that the differences between the contact profiles in the connectomes could be due to a large number of small, varying contacts. In the graph, a higher index number reflects a neuron with a higher amount of contact differences between L4 and adult. Red bars represent the differences between L4 and adult (178 neurons in total). Grey bars are the null difference distribution. Asterisks denote the location of single neurons that are hard to see on the graph. **f**, Same as in **e**, except the histogram represents distribution of differences in neuronal distances within the DC hierarchical outputs (Supplementary Methods section 'Diffusion Condensation Data Analysis'). Notably, we found that, unlike the contact adjacency data, the DC output clustering location was significantly similar in 127/178 neurons (71%) ($P < 0.05$), whereas only 9/178 neurons (5%) were significantly different than random ($P < 0.05$; by unpaired two-tailed Student's *t*-test between L4 vs. Adult and null distribution; df = 881,276, no adjustments were made for multiple comparisons; Supplementary Methods). These analyses, in the context of the differences seen for the contact profiles (**e**), indicate that the DC algorithm identifies meaningful relationships within the neuropil's tangled and varying contact profiles. **g**–**i**, C-PHATE plots of DC analyses preformed on adjacency matrices calculated using different contact thresholds for the L4 animal. Data presented in Fig. 1b was calculated with the 45 nm threshold. 45 nm is approximately 10 pixels in the EM datasets. DC correctly defines clusters even for the different thresholds. **j**–**l**, Same as in **g**–**i**, except for the adult animal. **m**, **n**, C-PHATE plots of the L4 and adult animal. The adult animal has 2 additional clusters at the highest modularity score. These clusters (shown in grey) are composed primarily of neurons that interact across multiple strata. Additionally, neurons from these smaller clusters in the adult also co-clustered in the L4 animal, but at an earlier iteration. Brackets indicate location of the cluster in the L4 and adult that is composed of similar neurons. The neurons within the cluster are listed between the two plots. **o**, **p**, C-PHATE plot of DC analyses preformed on the chemical synaptic connectomics data from the L4 animal (https://wormwiring.org). The C1 cluster, and part of the C3 cluster, are similar between the connectomic and contact DC analysis outputs. However, C2/C3/C4 are mixed in the connectomics DC output. **p** is a rotation of **o**, to show the partially retained C3 blue cluster, as seen at the top of the graph. Notably, we also found that the neuropil pioneers (Fig. 3i–k) that cluster in C2 in the contact DC analysis are now scattered among the different mixed clusters in the connectome DC analysis. The pioneering neurons SIA and SIB make almost no presynaptic contacts and very few postsynaptic contacts. This dispersion of the pioneers among different clusters in the connectome DC analysis highlights the value of using contact analysis to uncover the structural architecture of the neuropil, especially for neurons that are synaptically sparse. **q**–**s**, C-PHATE plots for the L4 animal (**q**), adult animal (**r**), and the adult animal where the neurons VB01 (and also HSNL and PVNR) were omitted from the adjacency matrices used to calculate the DC/C-PHATE plot (**s**). These are the only 3 neurons that are exclusively found in the adult because they haven't grown into the neuropil at the L4 stage. We observed that AVAR (C-PHATE plot location annotated with arrows) is assigned to Cluster 3 in the L4 animal and to Cluster 5 in the adult animal. AVAR makes extensive contacts with VB01 in the adult animal that are absent in L4 animal. We eliminated the VB01 neuron profile and contacts from the adult dataset and, consistent with our analyses, observed that AVAR now similarly clustered, as in the L4 dataset, to Cluster 3 in the adult dataset lacking VB01. This demonstrates that developmental differences affecting the contact profile of neurons leads to differences in the DC outputs between the L4 and adult animals. AVAR does not contact the other two neurons that were omitted in these analyses (HSNL and PVNR), suggesting that omission of VB01 is causative for the change in AVAR clustering. Graphs or plots in **a**, **c**, **g**–**i**, **m**, **o**–**q** are coloured according to the 4 clusters identified in iteration 23 of the L4 animal as in Fig. 1b using the 45 nm threshold: C1, red; C2, purple; C3, blue; C4, green. Graphs or plots in **b**, **d**, **j**–**l**, **n**, **r**, **s** are coloured according to the 6 clusters identified in iteration 22 of the adult animal using the 45 nm threshold: C1, red; C2, purple; C3, blue; C4, green; C5/6, grey.

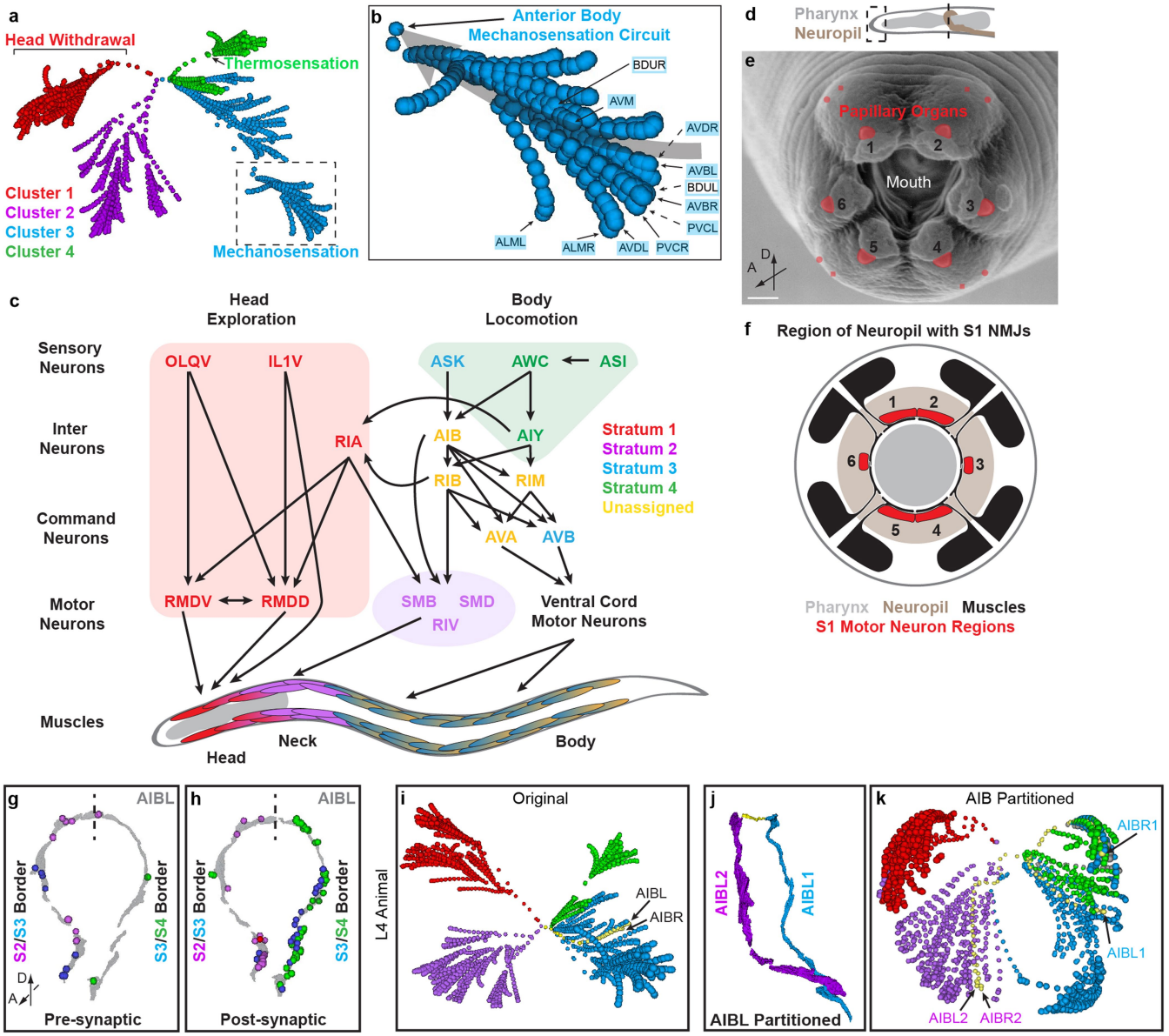

Extended Data Fig. 3 | See next page for caption.

Extended Data Fig. 3 | Examination of behavioural circuits in the DC/C-PHATE analyses. a, C-PHATE plot of DC analyses for a larval stage 4 (L4) animal, with known behavioural circuit locations highlighted. **b**, Enlargement of inset from **a** displaying the condensation of a group of neurons corresponding to the mechanosensation circuit[30,43,55,56]. Neurons with their names in filled blue boxes are members of the anterior body mechanosensation circuit, neurons with their names in outlined blue boxes (BDUL and BDUR) have been proposed to guide the formation of the circuit during development[56]. **c**, Model of functional segregation of information streams within the neuropil. Papillary sensory information is processed in S1 and innervates head muscles to control head movement. Amphid sensory information is processed in S3/S4 and links to body muscles (via command interneurons) and neck muscles (via motor neurons in S1/S2) to control body locomotion[29,38,42,57]. Interneurons cross strata to functionally link these modular circuits (Extended Data Fig. 5). Individual neuron classes and muscle outputs are coloured according to the strata they belong to (for muscles, according to the strata the innervating neurons belong to). **d**, Schematic of *C. elegans* head highlighting area in **e**, **f** as dashed rectangle and line, respectively. **e**, Representation of S1 sensory organs, projected over a scanning EM of the *C. elegans* mouth. Numbers highlight the sixfold symmetry of the papillary organs. Image produced by and used with permission of D. Hall. Mouth sensilla coloured according to their strata assignment. Scale bar, 1 µm. Same image as Fig. 2b. **f**, Topographical map of the S1 shallow head circuit. The S1 motor neurons, which have a 'fourfold-plus-two' symmetric pattern[39], make neuromuscular junctions (NMJs), projecting their symmetry onto the fourfold symmetrical muscle quadrants that control head movement (black)[39] (compare to **e** above). Numbers represent the fourfold-plus-two symmetry of the S1 neurons in (**e**). In brief, for example, for IL1 neurons, the dorsal and ventral IL1 neuron pairs (in our schematic, 1, 2 and 4, 5) connect to the dorsal and ventral muscle octants, while the lateral IL1 neurons connect to the two lateral muscle octants (in our schematic, 6 and 3 represent the two lateral IL1 neurons)[39]. **g**, **h**, Axial view of the 'rich-club' AIB left (AIBL) interneuron[15,20] (Fig. 2f) with distribution of the presynaptic (**g**) and postsynaptic (**h**) sites coloured according to the strata of the corresponding AIBL synaptic partner. The vertical dashed line indicates the division between proximal and distal regions of the neurite. Similar distribution was seen for AIB right (AIBR, not shown). **i**, C-PHATE plot of DC analysis for the larval stage 4 (L4) animal. AIBL/R are coloured yellow to highlight their location within the plot. **j**, Volumetric reconstruction of the unassigned (yellow), 'rich-club' AIBL interneurons[15,20] depicting the regions of AIB that were partitioned in the EM data. The proximal region is in blue (AIBL1), the lateral region in yellow and the distal region in purple (AIBL2). The proximal region of AIB borders S3/S4, and the distal region borders S2/S3 (Fig. 2f–i). **k**, C-PHATE plot of DC analysis for the larval stage 4 (L4) animal after AIBs had been partitioned in the EM dataset. AIB1s and AIB2s are yellow and the AIB lateral regions seen in **j** are grey. After partitioning the proximal regions (AIB1s) remain within C4, while the distal regions (AIB2s) now cluster with C2, demonstrating that DC/C-PHATE analysis clusters neurons on the basis of their neighbouring contact profiles. Plots in **a**, **b**, **i**–**k** are coloured according to the 4 clusters identified in iteration 23 of the L4 animal as in Fig. 1b: C1, red; C2, purple; C3, blue; C4, green.

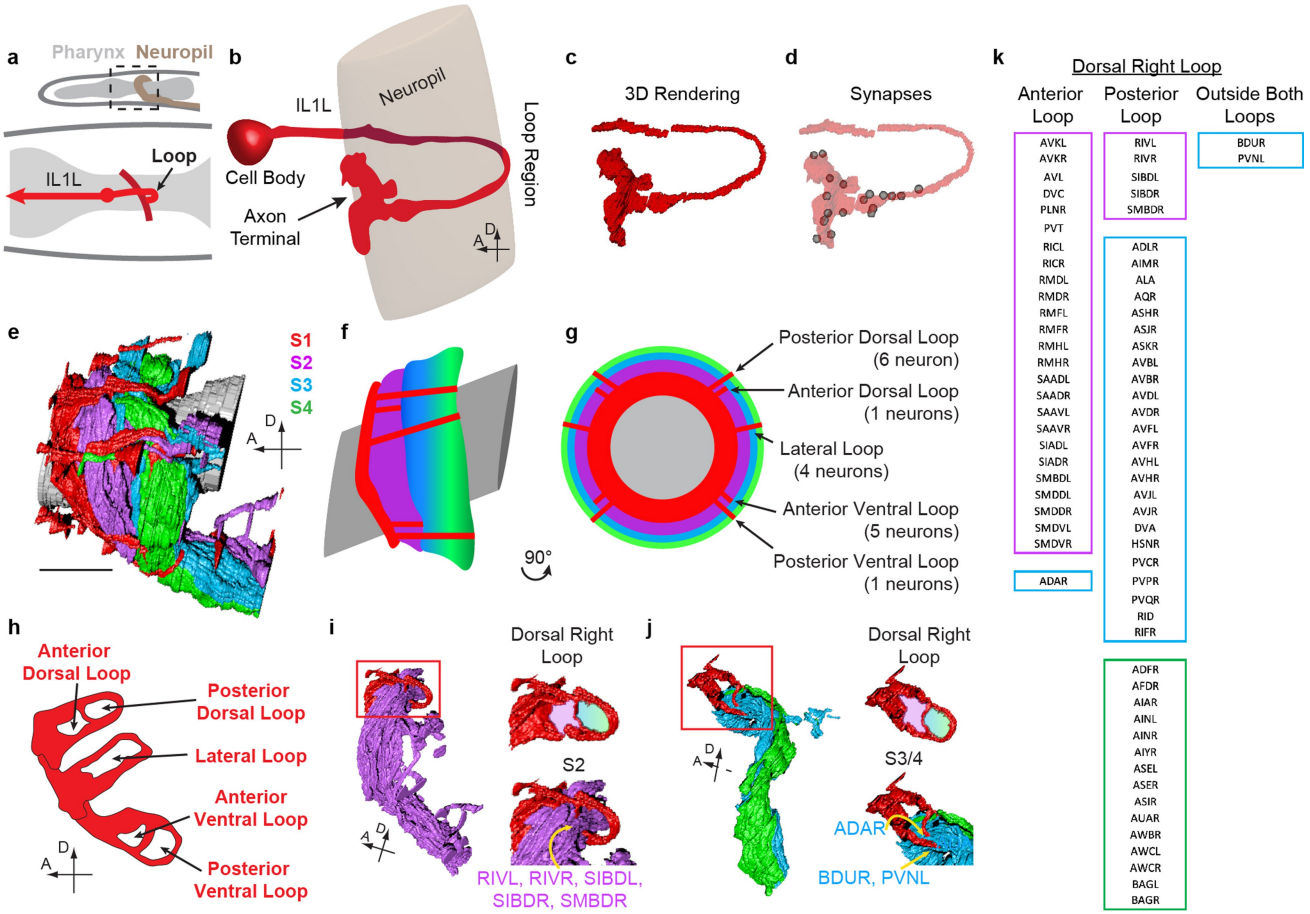

Extended Data Fig. 4 | S1 structure precisely encases S2, S3 and S4 of the neuropil. a, Illustration of the IL1L neuron based on data presented in ref. [3] (additional information available at https://wormatlas.org). Schematic of worm head and neuropil (dashed box) above. In the schematic below, the IL1 neuron is in red, with dendrite (left pointing arrow), soma (circle) and axon (right pointing loop, arrow). The pharynx (shaded grey) is shown for reference. **b**, Cartoon of IL1L loop in the context of the nerve ring neuropil (sensory dendrite not shown). **c**, Volumetric reconstruction of IL1L from L4 animal EMs. **d**, Overlay of IL1L volumetric reconstruction and synapses (grey spheres) highlighting the position of the synaptic endplate (after the neuron loops around the neuropil). **e**, Volumetric reconstruction of the L4 neuropil with individual neurons from the 4 strata coloured as follows: S1, red; S2, purple; S3, blue; S4, green). Scale bar, 5 µm. **f**, **g**, Schematic of the structure formed by the S1 looping structures, from a lateral (**f**) and axial (**g**) view with neuropil strata. **h**, Schematic of the S1 loops (lateral view) without the strata (as Fig. 1d). **i**, **j**, Volumetric reconstruction of dorsal right loop and S2 (**i**) and S3/S4 (**j**) with individual neurons that fall outside of the looping structure rule (yellow arrows). Although 90% of S2, 84% of S3 and 100% of S4 neurons are contained within the indicated loops, a minority of neurons belonging to S2 and S3 strata are not encased by the loops corresponding to the specific strata. We include the names of these neurons below the volumetric reconstructions; Supplementary Video 5. **k**, List of all neurons and their positions in the dorsal right loop structures, coloured according to the 4 strata (a complete listing of all neurons, and their positions within the sixfold symmetric honeycomb structure, can be found in Supplementary Table 1, and movie projections of the honeycomb-like structure in the context of the strata in Supplementary Videos 4, 5).

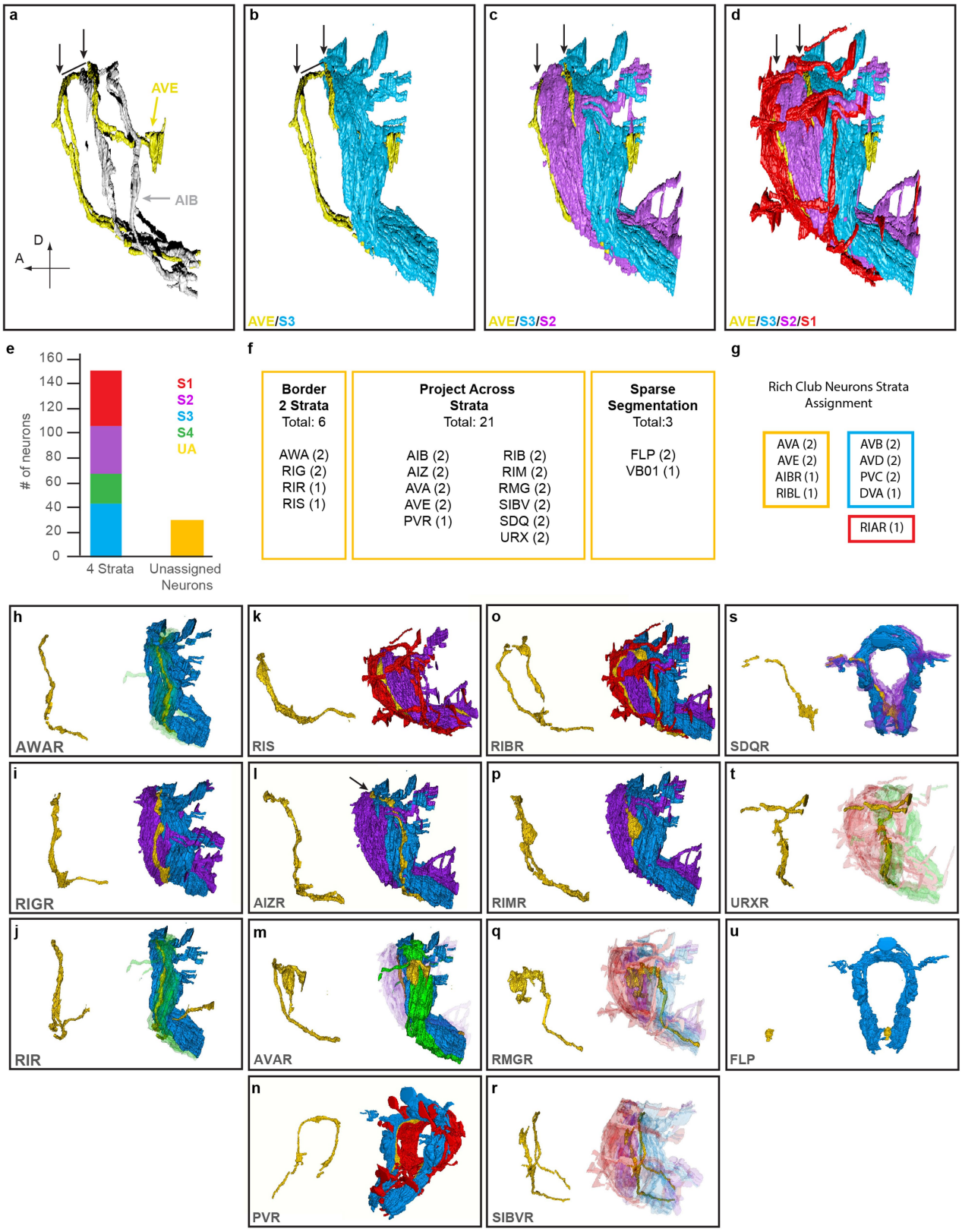

Extended Data Fig. 5 | See next page for caption.

Extended Data Fig. 5 | Neurons unassigned to the 4 strata anatomically contact multiple strata, and a subset belong to the highly interconnected 'rich-club' neurons. a–**d**, Volumetric reconstructions of the unassigned AVE interneuron (yellow) in the context of nerve ring strata, with AIB (grey). Arrows indicate the two segments of AVE that border strata. AVE has a similar morphology to AIB (Fig. 2f) but is anteriorly displaced by one stratum: AVE borders S2/S3 (**b**, **c**), shifts along the A–P axis, and then borders S1/S2 (**c**, **d**). Lines in **a**, **b** indicates AVE shift along the A–P axis to shift strata; Supplementary Video 7. **e**, Analysis of the total number of neurons within each stratum, and in the unassigned group. **f**, Classification of 'unassigned' neurons. **g**, Stratum location of the rich club neurons[15,20]. Coloured box depicts strata assignment. These 14 neurons functionally consist of two groups: eight command interneurons (which modulate the backward and forward locomotion; AVA, AVB, AVD, PVC) and six nerve ring interneurons (AVE, AIBR, RIBL, RIAR, DVA). The six command interneurons that are not part of the unassigned group have neurites that remain within S2. The two command interneurons that are part of our unassigned group (AVA) border S2 and S3, and contain a large protrusion that crosses S3/S4 (Extended Data Fig. 5m). Of the six 'rich-club' interneurons, four of them were identified in our DC analyses as neurons that cross strata. One that was not identified in our analysis is RIAR, but it is a neuron that also crosses between S1 and S4. As such, our study extends the understanding of the rich-club interneurons in the context of the nerve ring, particularly the subgroup of rich-club interneurons that are not part of the command interneurons. **h**–**u**, Volumetric reconstructions of all unassigned neurons highlighting their strata interactions. **h**, AWA borders S3/S4. **i**, RIG borders S2/S3. **j**, RIR borders S3/S4. **k**, RIS borders S1/S2. **l**, AIZ shifts perpendicularly from S3 to the S2/S3 border, highlighted with arrow. **m**, AVA borders S2/S3 and protrudes into S3 and S4. **n**, PVR borders S1/S3 and protrudes into S1. **o**, RIB forms a cage-like structure around S2. **p**, RIM borders S2/S3 and protrudes into S3. **q**, RMG protrudes into S1/S2/S3. **r**, SIBV's main neurite is in S2, but it sends a second neurite into S1. **s**, SDQ borders S2/S3. **t**, URX interacts with S1 and S4. **u**, FLP has sparse segmentation data in the nerve ring. Images are rotated relative to each other, and transparency settings vary between images, for clarity in display of their position within the nerve ring. Neurons are arranged according to **f**.

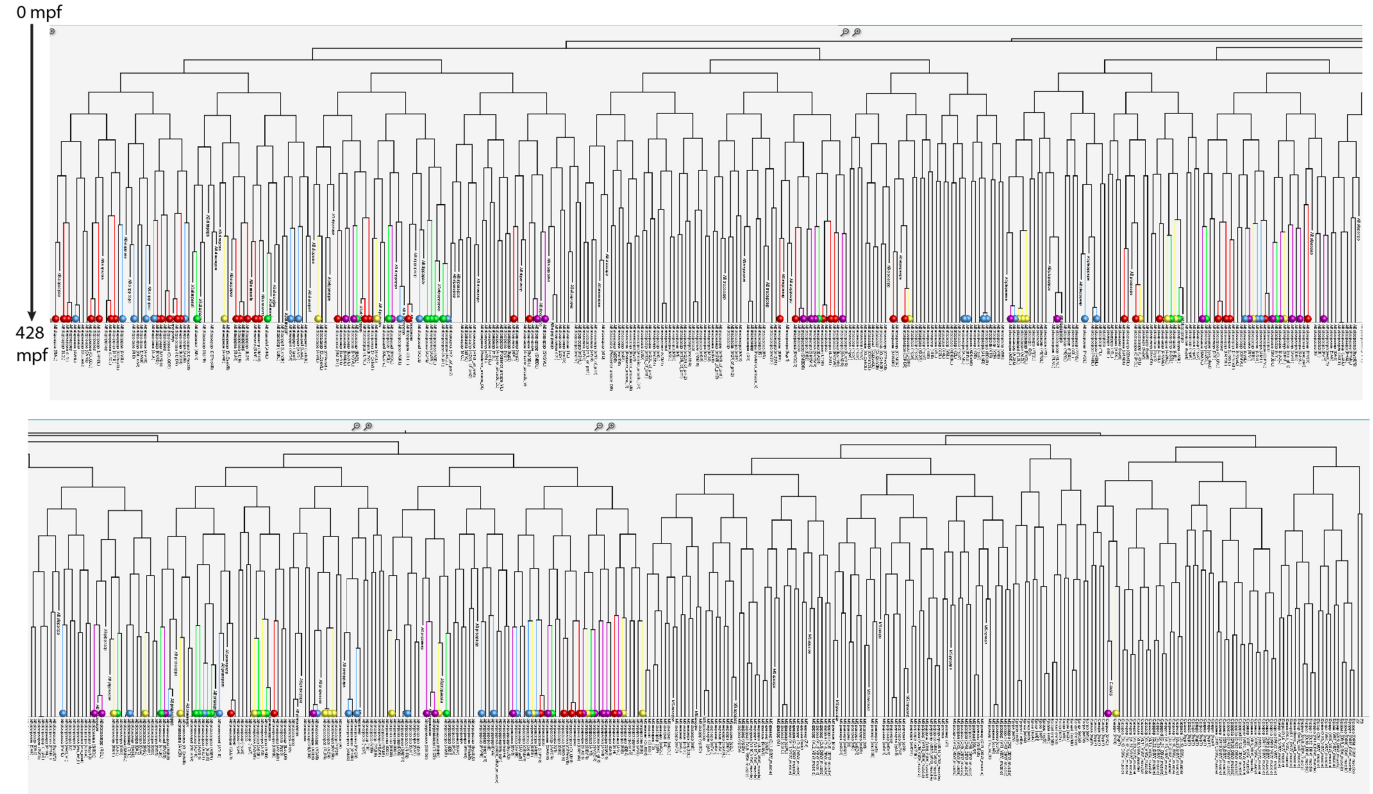

Extended Data Fig. 6 | Analysis of the 4 strata in the context of the lineage tree. Lineage tree for *C. elegans* (0–428 mpf). The terminal branch of each neuron is coloured according to its stratum assignment and marked with a similarly coloured sphere. The lower panel is part of the lineage tree above. Upon detailed examination of all 181 neuropil neurons in the context of the lineage tree, although we observe clusters of neurons, we could not systematically correlate those clusters (representative of terminal lineage positions) with stratum assignment. This image was generated using WormGUIDES[51]. For access to a fully interactive lineage tree, see Supplementary Discussion 1.

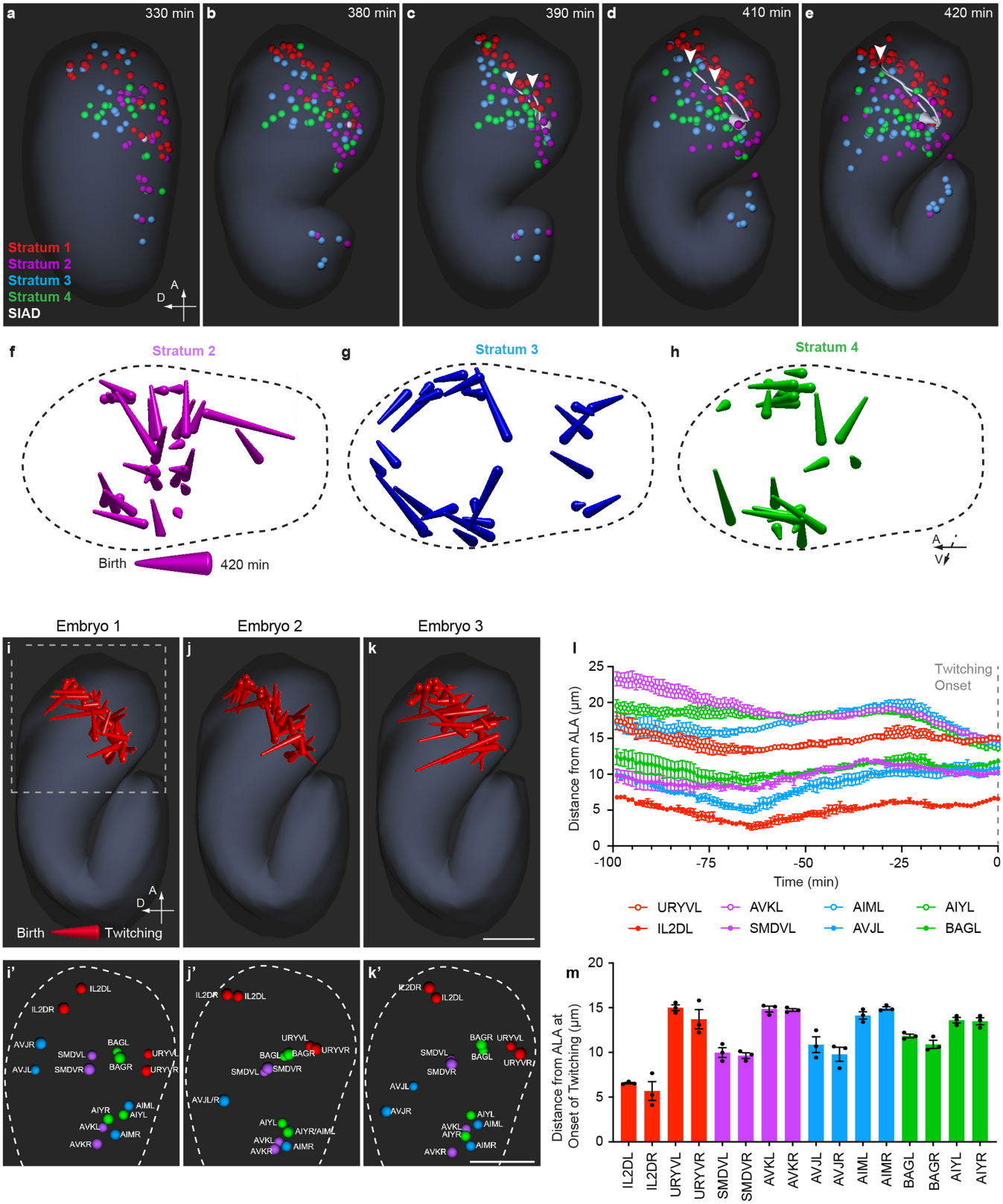

Extended Data Fig. 7 | See next page for caption.

Extended Data Fig. 7 | Early stereotypical segregation of neuronal somas correlates with neuropil strata architecture. a–**e**, Time series of neuronal soma positions within the embryo (generated using WormGUIDES[51]). We analysed soma positions from around 0 to 430 mpf; during this interval the embryo proceeds through gastrulation, into the early stages of elongation, and the majority of the terminal neuronal cell divisions are completed. We found that soma segregation occurs between 330–420 mpf. S2 pioneer neuron, SIAD, is shown in white for reference of nerve ring position. White arrowheads in **c**, **d** highlight the growing tips of the pioneer SIAD. The white arrowhead in **e** highlights the dorsal midline (meeting point for the bilateral SIADs). S1 somas are anteriorly segregated before pioneer neurite outgrowth (Supplementary Video 8). **f**–**h**, 3D depth trajectories displaying the movement of cells that will extend their neurites to S2 (**f**), S3 (**g**) or S4 (**h**) (movement represented from neuronal cell birth to 420 mpf). S2 movement has a ventral bias. S3 movement is principally along the outermost embryonic edge, and S4 clusters into 2 bilaterally symmetric groups. **i**–**k**, 3D depth trajectories of S1-cell movements between neuronal cell birth and 420 mpf for 3 different lineaged embryos. The embryo in **i** is the same dataset as the embryo shown in **a**–**h**) and in Fig. 3b–d. The migration trajectories for all 3 embryos is stereotypical. The dashed box highlights the area shown in **i'**–**k'**. Scale bar (10 µm) applies to **i**–**k**. **i'**–**k'**, Neuronal soma positions for cells from the four strata just before twitching onset. Same embryos as in **i**–**k**. Similar to the migration trajectories (**i**–**k**) the positions of neuronal somas from each stratum are stereotypical across individuals. Scale bar (10 µm) applies to **i'**–**k'**. **l**, Quantifications of average 3D distances from selected neuronal somas to the ALA neuron soma over a 100 min interval up to the start of twitching (430 mpf). ALA was used as reference because its position was reported to be reproducible between individual embryos[58]. The migration paths for neurons from the 4 strata are stereotypical across animals, and we found that the average neuron's 3D distance from ALA varies by a standard deviation of less than a micrometre (~0.73 µm). **m**, Quantification of average 3D distances from selected neuronal somas to the ALA neuron soma just before the onset of twitching (430 mpf). Neuron somas in all panels are coloured according to strata assignment (S1, red; S2, purple; S3, blue; S4, green). For **l**–**m**, means are from 3 embryos (same embryos as in **i**–**k'**). All error bars are mean ± s.e.m.

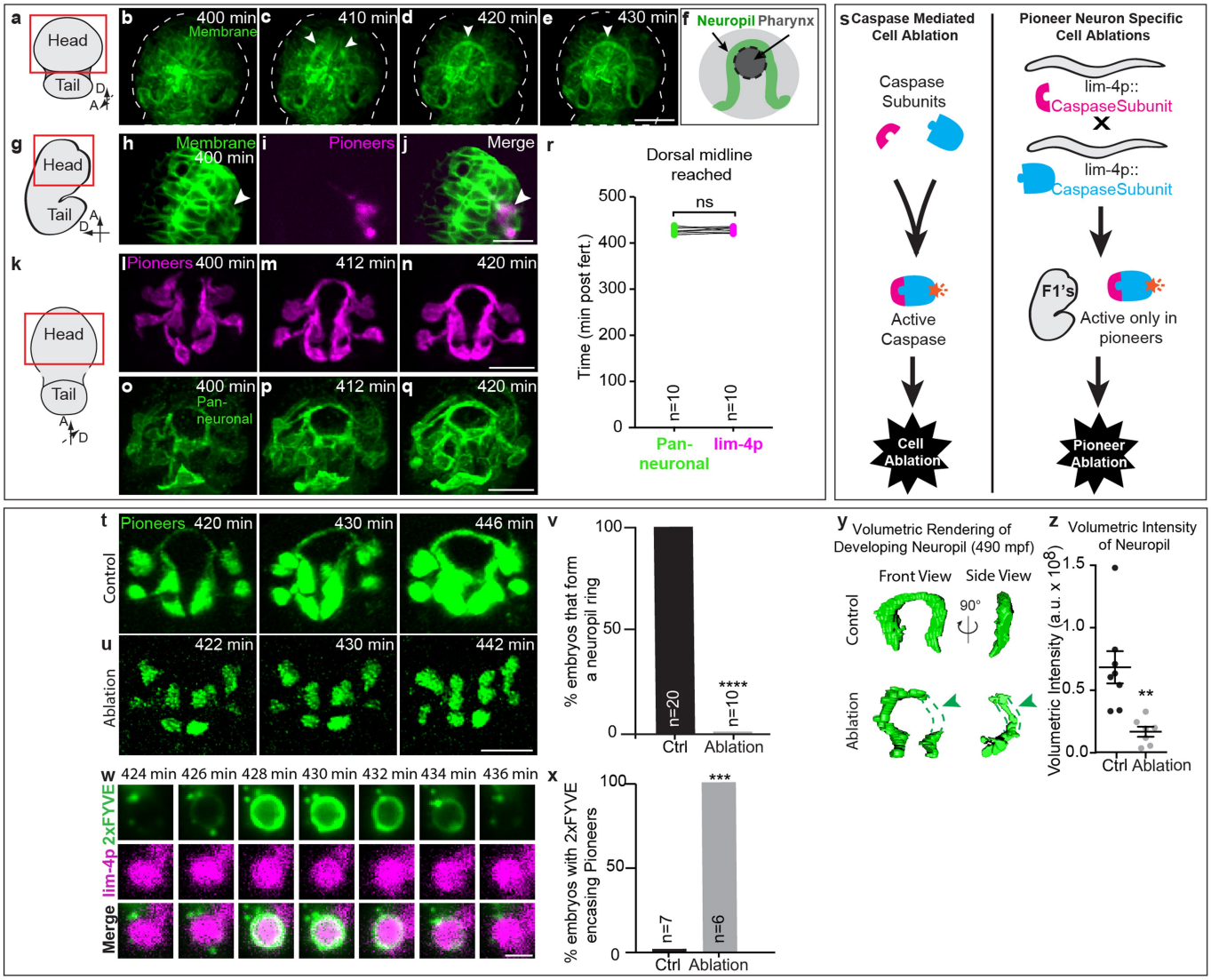

Extended Data Fig. 8 | See next page for caption.

Extended Data Fig. 8 | S2 pioneering neurons outgrowth initiate development of the stratified neuropil and are required for nerve ring neuropil development. a, Schematic of *C. elegans* embryo depicting region displayed in **b**–**f**, red box. **b**–**f**, Time-lapse of the outgrowth dynamics of the neuropil (labelled with ubiquitous *nhr-2p::membrane-tethered::gfp*) and schematic. Arrowheads indicate first extensions entering the future neuropil. Deconvolved diSPIM maximum intensity projections are shown ($n = 8$ embryos; Supplementary Video 9). **g**, Schematic of *C. elegans* embryo depicting region displayed in **h**–**j**, red box. **h**–**j**, Comma stage embryo (400 mpf) co-labelled with ubiquitous (*nhr-2p::membrane-tethered::gfp*) and pioneer neuron (*lim-4p::mCherry*) markers. Membrane and pioneer expression co-localize in SIAD, SIBV, and SMDD confirming the lineaging analysis (Fig. 3e–h). Single *z*-slice acquired with a single diSPIM arm shown ($n = 12$ embryos). The arrow indicates co-labelling of the two markers. **k**, Schematic of *C. elegans* embryo depicting the region displayed in **l**–**n**, **o**–**q**, red box. **l**–**n**, Time-lapse of the outgrowth dynamics of pioneer neurons (labelled with *lim-4p::membrane-tethered::gfp*). The same image series was used in Fig. 3i, j and are displayed here for comparison with the next panels. Deconvolved diSPIM maximum intensity projections are shown ($n = 16$ embryos). **o**–**q**, Time-lapse of the outgrowth dynamics of the neuropil (labelled with *rab-3p::membrane-tethered::gfp*). Deconvolved diSPIM maximum intensity projections are shown ($n = 3$ embryos). Neuronal outgrowth into the neuropil occurs simultaneously for pioneers (**l**–**n**) and the first pan-neuronal outgrowth events detected (**o**–**q**), suggesting the S2 pioneers are the first to enter the developing neuropil (Supplementary Video 11). **r**, Analysis of timing for arrival to the dorsal midline in a strain co-labelled with *rab-3p::membrane-tethered::gfp*, and *lim-4p::mCherry*. Points connected with a line correspond to data points from the same embryo ($n = 10$ embryos). ns, not significant by paired two-tailed Student's *t*-test. **s**, Schematic of caspase ablation strategy for pioneer neurons. The left panel depicts split-caspase induced cell ablation, as described in ref. [53]. The right panel depicts pioneer-specific split-caspase ablation assay in embryos. The *lim-4p* promoter was used to drive caspase expression in the SIA, SIB, SMD, RIV and SAAV neurons, ablating them before neurite outgrowth. F1 is first generation after mating. **t**, **u**, Time-lapse of the outgrowth dynamics of the pioneering neurons in control (**t**) and pioneer ablated (**u**) embryos (labelled with *lim-4p::mCherry*). Pixel intensities are different for **t** and **u** owing to a significant decrease in signal in the ablated animals. Deconvolved diSPIM maximum intensity projections are shown (Ctrl, $n = 20$ embryos; Ablation, $n = 10$ embryos). Previous studies showed that laser-ablations of subsets of these pioneer neurons were wild-type[59], suggesting the existence of functional redundancy in guiding nerve ring development. **v**, Quantification of the percentage of embryos forming a full neuropil ring in control and pioneer-ablation embryos. *n* = number of embryos scored. $^{****}P < 0.0001$ by two-sided Fisher's exact test between control and ablation. **w**, Time-lapse of the dynamics of 2xFYVE on ablated pioneering neuron somas. 2xFYVE is a marker of cell death and appears around cell corpses as described[60]. To see cell corpses of pioneer neurons, embryos were labelled with *ced-1p::2xFYVE::gfp(S65C/Q80R)* (to image cell corpses) and *lim-4p::mCherry* (to image pioneer neurons). Single *Z*-plane from diSPIM dataset shown (ctrl, $n = 7$ embryos; ablation, $n = 6$ embryos). **x**, Quantification of 2xFYVE encasing ablated pioneer somas. $^{***}P = 0.0006$ by two-sided Fisher's exact test between control and ablation. *n* = number of embryos scored. **y**, Volumetric reconstruction of the developing neuropil for control and pioneer ablated embryos. Volumes were acquired from diSPIM images analysed with 3D Object Counter (FIJI-ImageJ2; Supplementary Methods). Green arrowheads emphasize aberrant neuropil phenotypes in ablation animals (gaps in the neuropil and decreased widths). **z**, Analysis of pixel intensity within the neuropil volume of control and pioneer ablated embryos. Each dot represents the summation of all pixels within a neuropil volume for 1 embryo (Ctrl, $n = 8$; ablation, $n = 7$), quantified using 3D Object Counter (FIJI-ImageJ2; Supplementary Methods). $^{**}P = 0.0032$ by two-tailed Student's *t*-test between control and ablation. Error bars are mean ± s.e.m. Timing for all panels is mpf. Scale bar, 10 µm (**b**–**e**, **h**–**j**, **l**–**n**, **o**–**q**, **t**, **u**); 3 µm (**w**).

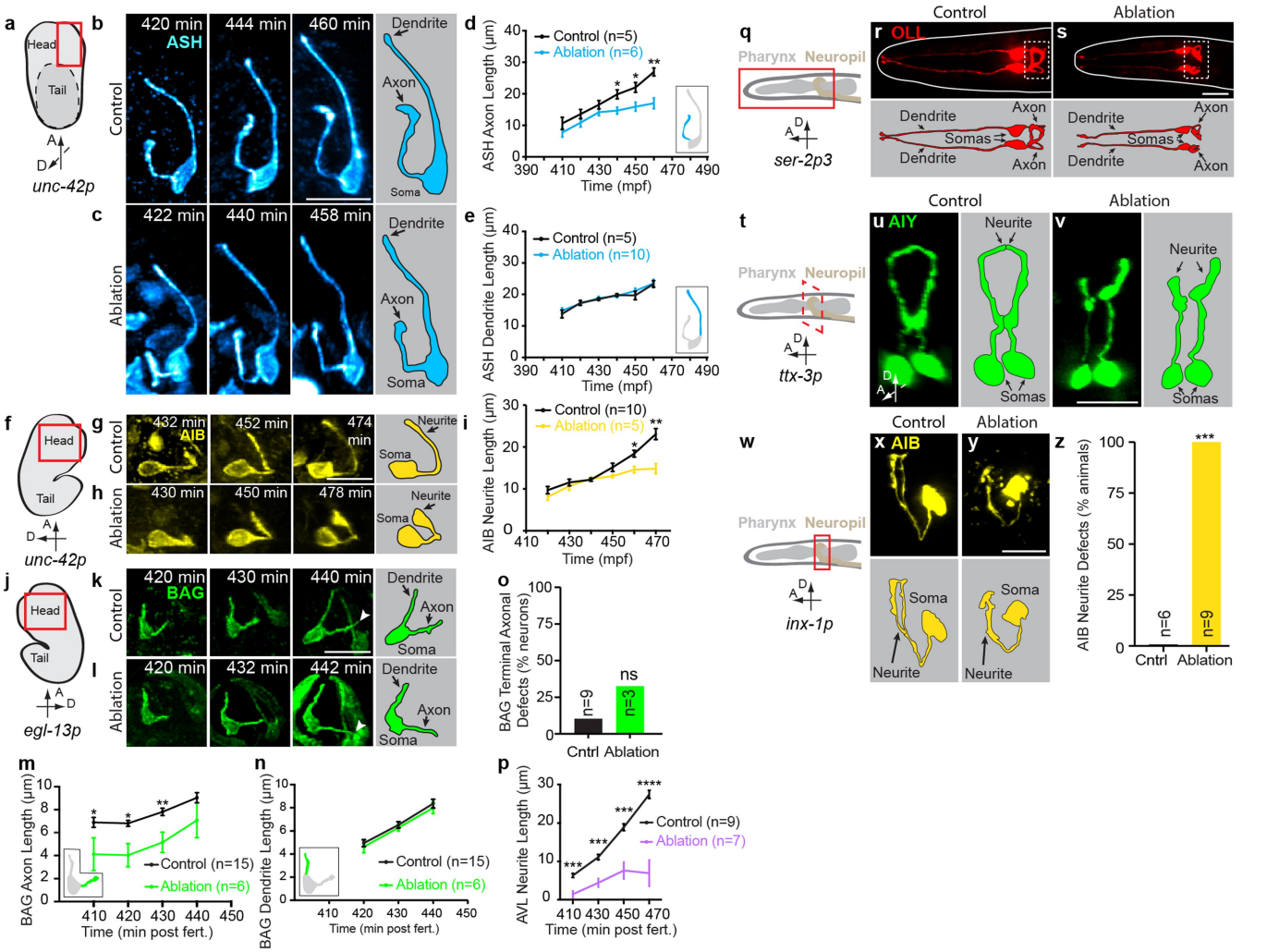

Extended Data Fig. 9 | S2 pioneer neurons are required for the development of neurons from all four strata, and the unassigned neurons. a, Schematic of embryo, highlighting area in **b**, **c** with a red rectangle. Promoters used are shown below schematic in italics. **b**, **c**, Time-lapse of outgrowth dynamics of stratum 3 neuron ASH in control (**b**) and pioneer-ablated (**c**) embryos, with schematic (right). Deconvolved diSPIM maximum intensity projections shown (Ctrl, $n = 5$ neurons; ablation, $n = 6$ neurons; Supplementary Video 14). **d**, **e**, Quantifications of ASH axon (**d**) or dendrite (**e**) outgrowth for control and ablated animals. Axons (which are in the nerve ring) are affected by nerve ring pioneer neuron ablations, whereas dendrites (which are not in the nerve ring) are not affected. n = number of neurons quantified. $^{*}P < 0.05$, $^{**}P < 0.01$, $^{***}P < 0.001$, $^{****}P < 0.0001$ by unpaired two-tailed Student's t-test between control and ablation at each time point (see Supplementary Methods for exact P values). Time points without annotation are not significant. Error bars are mean ± s.e.m. **f**–**i**, As for **a**–**d**, but for unassigned interneuron AIB (Ctrl, $n = 10$ neurons; ablation, $n = 5$ neurons; Supplementary Video 15). **j**–**n**, As for **a**–**e**, but for S4 neuron BAG (Ctrl, $n = 15$ neurons; ablation, $n = 6$ neurons;). **o**, Quantification of the percentage of BAG neurons with defective morphologies at 444 mpf for control and pioneer-ablated animals. BAG neurons are delayed in early outgrowth, but eventually find their terminal locations, suggesting guidance of this neuron relies on redundant mechanisms. n = number of embryos. ns indicates not significant by two-sided Fisher's exact test between control and ablation. **p**, As for **d** but for S2 neuron AVL shown in (Fig. 4d, e). **q**, Schematic of *C. elegans* head highlighting area in **r**, **s** as red rectangle. **r**, **s**, Larval stage 1 (L1) images of S1 neuron OLL in control and pioneer-ablated animals, with schematic (below). L1 images were taken because there were no available promoters to image OLL in embryos. Spinning disk confocal maximum intensity projections shown (Ctrl, $n = 8$ animals; ablation, $n = 20$ animals). **t**–**v**, As for **q**–**s** but for S3 neuron AIY (Ctrl, $n = 10$ animals; ablation, $n = 16$ animals). **w**–**y**, As for **q**–**s** but for unassigned neuron AIB (Ctrl, $n = 6$ animals; ablation, $n = 9$ animals). The AIB outgrowth defect in embryogenesis (**h**) persists to L1 (**y**). **z**, Quantification of the percentage of AIB neurons with defective morphologies in L1 animals for control and pioneer-ablated animals. n = number of animals scored. $^{***}P = 0.0002$ by two-sided Fisher's exact test between control and ablation. For cell-specific labelling of neurons, see Supplementary Methods and Supplementary Tables 2, 3. Scale bar, (**b**, **c**, **g**, **h**, **k**, **l**, **r**, **s**, **u**, **v**, **x**, **y**) 10 µm; and timing for all panels is mpf. Neurons are coloured according to which strata they belong to (S1, red; S2, purple; S3, blue; S4, green; unassigned, yellow).

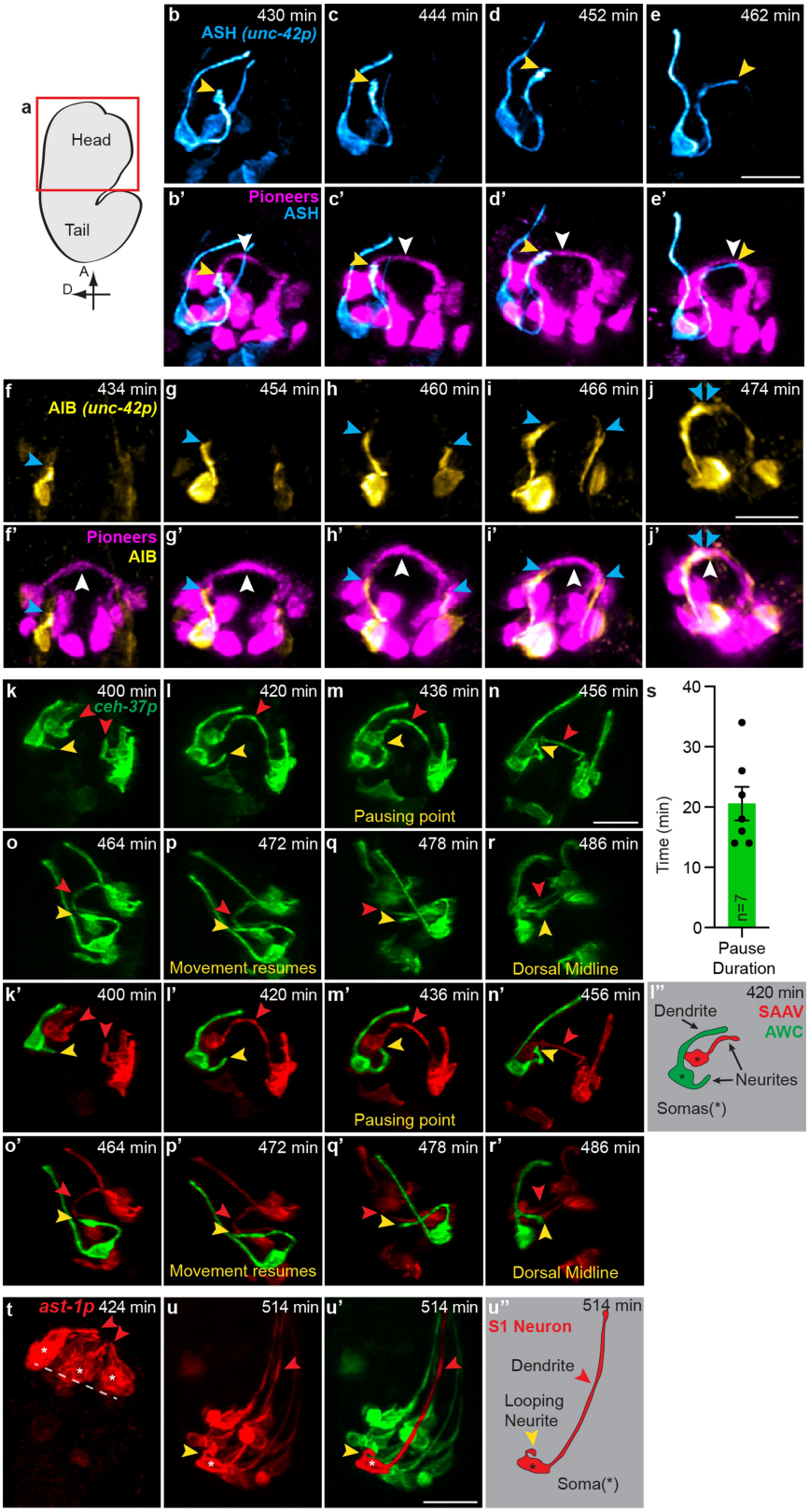

Extended Data Fig. 10 | See next page for caption.

Extended Data Fig. 10 | A temporal progression of outgrowth, beginning with the S2 pioneers, results in the inside-out development of the nerve ring. a, Schematic of embryo, highlighting area in **b**–**u** with a red rectangle. **b**–**e**, Time-lapse of the outgrowth dynamics of S3 neuron ASH in control animal. For ASH cell-specific labelling, see Supplementary Methods. **b'**–**e'**, As **b**–**e** but includes S2 pioneer neurons (labelled with *lim-4p::mCherry*). Yellow arrowheads mark ASH axonal outgrowth in the context of the pioneers. White arrowheads mark dorsal midline. ASH outgrowth into the neuropil occurs after the pioneers have grown into the nerve ring. Deconvolved diSPIM maximum intensity projections shown ($n = 4$ embryos). **f**–**j**, Time-lapse of the outgrowth dynamics of unassigned neuron AIB in control animal. For AIB cell-specific labelling, see Supplementary Methods. **f'**–**j'**, As **f**–**j**, but includes S2 pioneer neurons (labelled with *lim-4p::mCherry*). Blue arrowheads mark AIB axonal outgrowth in the context of the pioneers. White arrowheads mark the dorsal midline. AIB enters the neuropil after the pioneers have reached the dorsal midline, and as ASH reaches the dorsal midline (compare **e'** to **h'**). Data collected in this way **b**–**j** were used for indicated neurons in Fig. 4j. Deconvolved diSPIM maximum intensity projections shown ($n = 6$ embryos). **k**–**r**, Time-lapse of the outgrowth dynamics for S2 pioneer SAAV, and S4 neuron AWC. In **k**, red arrowheads mark outgrowth of SAAV. In **l**–**r**, red arrowheads mark the dorsal midline and yellow arrowheads mark the outgrowth of AWC. The S4 neuron AWC pauses for around 20 min near the SAAV soma before growing into the nerve ring. Deconvolved diSPIM maximum intensity projections shown. $n = 7$ embryos. The *ceh-37p* promoter expresses strongly in SAAV and AWC, but weakly in ADF, AFD, AWB. **k'**–**r'**, As **k**–**r**, but one side of the bilateral AWC neurons have been pseudocoloured green and the remaining image pseudocoloured red to highlight the outgrowth of the S4 neurons ($n = 7$ embryos; Supplementary Methods). **l''**, Schematic of **l'** depicting the growing SAAV (red) and AWC (green) neuron. **s**, Quantification of AWC pausing duration. Each dot represents an embryo ($n = 7$). AWC pauses at the SAAV cell body for around 20 min before entering the neuropil. Error bars are mean ± s.e.m. (see Supplementary Methods for quantification). **t**, **u**, Time-lapse of the outgrowth dynamics for S1 sensory neurons. Red arrowheads mark sensory endings. The yellow arrowhead marks outgrowth of a looping neuron. The dashed line in **t** corresponds to the position of the pioneering neurons (seen in Fig. 3i, j). The outgrowth of looping structures starts after 420 min, that is, after the pioneer neurons have grown out (compare to Fig. 3i, j). Image in **u** taken in a threefold embryo, which moved (therefore position of cell bodies is different between **t** and **u**). Deconvolved diSPIM maximum intensity projections shown. ($n = 9$ embryos; compare to Fig. 4j). **u'**, As **u**, but one S1 sensory neuron has been pseudocoloured red and the remaining image pseudocoloured green to highlight the looping outgrowth of the S1 neuron (Supplementary Methods). **u''**, Schematic of **u'** depicting the growing loop of the S1 sensory neuron. Together with the temporal dynamics of outgrowth and the ablation studies, our findings support an inside-out model in which the strata are assembled through timed entry into the nerve ring, starting with a core unit of the pioneering bundle, proceeding to central S2, then to the peripherally located neurons in S1 (anterior) and S4 (posterior), followed by outgrowth of neurons which link the strata, such as the S1 looping neurons or the neurons that cross strata (like AIB). Scale bar, 10 µm (**b**–**e'**, **f**–**j'**, **k**–**r'**, **t**–**u'**), and timing for all panels is mpf. The promoter used to drive expression is shown in italics in **b**, **f**, **k**, **t**.

nature research

Corresponding author(s): Daniel Colon-Ramos

Last updated by author(s): Oct 26, 2020

Reporting Summary

Nature Research wishes to improve the reproducibility of the work that we publish. This form provides structure for consistency and transparency in reporting. For further information on Nature Research policies, see our Editorial Policies and the Editorial Policy Checklist.

Statistics

For all statistical analyses, confirm that the following items are present in the figure legend, table legend, main text, or Methods section.

n/a	Confirmed	
☐	☒	The exact sample size (*n*) for each experimental group/condition, given as a discrete number and unit of measurement
☐	☒	A statement on whether measurements were taken from distinct samples or whether the same sample was measured repeatedly
☐	☒	The statistical test(s) used AND whether they are one- or two-sided *Only common tests should be described solely by name; describe more complex techniques in the Methods section.*
☒	☐	A description of all covariates tested
☐	☒	A description of any assumptions or corrections, such as tests of normality and adjustment for multiple comparisons
☐	☒	A full description of the statistical parameters including central tendency (e.g. means) or other basic estimates (e.g. regression coefficient) AND variation (e.g. standard deviation) or associated estimates of uncertainty (e.g. confidence intervals)
☐	☒	For null hypothesis testing, the test statistic (e.g. *F*, *t*, *r*) with confidence intervals, effect sizes, degrees of freedom and *P* value noted *Give P values as exact values whenever suitable.*
☒	☐	For Bayesian analysis, information on the choice of priors and Markov chain Monte Carlo settings
☒	☐	For hierarchical and complex designs, identification of the appropriate level for tests and full reporting of outcomes
☒	☐	Estimates of effect sizes (e.g. Cohen's *d*, Pearson's *r*), indicating how they were calculated

Our web collection on statistics for biologists contains articles on many of the points above.

Software and code

Policy information about availability of computer code

Data collection	diSPIM was operated with Micro Manager (1.4) available at https://micro-manager.org/. FIJI (ImageJ2) was used for EM segmentation. EM adjacency analysis code available at https://github.com/cabrittin/volumetric_analysis. MIPAV (V7.3) was used to deconvolve embryos for Ex. Data Fig. 7.
Data analysis	Diffusion condensation code available at https://github.com/agonopol/worm_brain. DC code run using MATLAB (R2017b). C-PHATE code available at dccphate.wormguides.org/CPHATE_pythonCode.zip. Lineage Software StarryNite (SN_FeederV1) and AceTree (16bitCompat) available at http://dispimlineage.wormguides.org/. FIJI (Image2) used for data analysis. CytoSHOW (V1) used for data analysis, available at http://run.cytowshow.org/. Adobe Photoshop (2020 21.0.1) was used for pseudo-coloring of images detailed in Methods. GraphPad Prism (8.2.0) used for statistical analysis. Microscopy Image Browser (MIB-V2.511) and 3dmod (IMOD-V4.9.12) were used to generate Sup. Video 3.

For manuscripts utilizing custom algorithms or software that are central to the research but not yet described in published literature, software must be made available to editors and reviewers. We strongly encourage code deposition in a community repository (e.g. GitHub). See the Nature Research guidelines for submitting code & software for further information.

Data

Policy information about availability of data

All manuscripts must include a data availability statement. This statement should provide the following information, where applicable:

- Accession codes, unique identifiers, or web links for publicly available datasets
- A list of figures that have associated raw data
- A description of any restrictions on data availability

The datasets generated during and/or analyzed during the current study are available from the corresponding author upon request. To facilitate exploration of the placement of neurites in the C-PHATE diagrams we generated a 3D interactive version of the C-PHATE plots. Plots can be downloaded, and neurite condensation

and position can be examined. These 3D interactive versions allow for identification of any neuron within the C-PHATE plot and provide iteration # and total neurons found within any cluster (See Supplementary Discussion 2 for instructions on how to access the data.)

Field-specific reporting

Please select the one below that is the best fit for your research. If you are not sure, read the appropriate sections before making your selection.

☒ Life sciences ☐ Behavioural & social sciences ☐ Ecological, evolutionary & environmental sciences

For a reference copy of the document with all sections, see nature.com/documents/nr-reporting-summary-flat.pdf

Life sciences study design

All studies must disclose on these points even when the disclosure is negative.

Sample size	The sample sizes used in the study are indicated in the figure legends, in the figure graphs or both. Sample sizes used were determined based on prior work from similar studies such as (Rapti et al. Nat Neurosci 20, 1350-1360, (2017) & Shah et al. Developmental Cell 43, 530-540 (2017)). Appropriate statistical tests were done based on the sampling number. No statistical test was used to determine appropriate sample size. To select sample sizes we noted that: 1) The phenotypes examined have large effect sizes. The sample size we chose is in excess for the power calculations, but we selected the sample size to capture the richness of the examined phenotypes in the populations of C. elegans worms and because of the practical ease with which substantial number of C. elegans can be examined, and the benefits those observations convey to the study. As indicated in methods, scoring was done blindly where possible. Scoring was done across different days, and by examining/noting developmental stages, to control for variables that might affect the robust phenotypes observed. 2) C. elegans development is stereotypic (Sulston et al. Developmental Biology 100, 64-119, (1983) & White et al. Philos Trans R Soc Lond B Biol Sci 314, 1-340, (1986)). In our experiments the results were steroytpic and reproducible.
Data exclusions	For Fig. 4c and Extended Data Fig. 6h a single control embryo was excluded because it was incorrectly segmented in our automated thresholding protocol, likely due to problems with the array expression. Failure in segmentation prevented failure in quantification, so this embryo was excluded from further analysis. No other data was excluded in this study.
Replication	All experiments contained at least 3 biologically independant samples and all attempts at replication were successful.
Randomization	Animals were randomly selected for experimentation.
Blinding	Investigators performed blind analysis when possible. Due to severe phenotypes generated after cell ablations, blind group allocation during data collection was not possible, but all embryos imaged (control and ablations) were collected using similar preparation and imaging conditions. Also, the severe ablation phenotypes made it impossible to blind investigators during image analysis, but analysis was preformed identically for control and ablation animals.

Reporting for specific materials, systems and methods

We require information from authors about some types of materials, experimental systems and methods used in many studies. Here, indicate whether each material, system or method listed is relevant to your study. If you are not sure if a list item applies to your research, read the appropriate section before selecting a response.

Materials & experimental systems

n/a	Involved in the study
☒	☐ Antibodies
☒	☐ Eukaryotic cell lines
☒	☐ Palaeontology and archaeology
☐	☒ Animals and other organisms
☒	☐ Human research participants
☒	☐ Clinical data
☒	☐ Dual use research of concern

Methods

n/a	Involved in the study
☒	☐ ChIP-seq
☒	☐ Flow cytometry
☒	☐ MRI-based neuroimaging

Animals and other organisms

Policy information about studies involving animals; ARRIVE guidelines recommended for reporting animal research

Laboratory animals	C. elegans strains were used in this study. Genetic details available in Supplementary Table 2. C. elegans animals analyzed were hermaphrodites at the developmental stages indicated in the text and Methods (Adult, L4, L1, and embryos).
Wild animals	Study did not involve wild animals.
Field-collected samples	Study did not involve samples collected from the field.

Ethics oversight	No ethical approval was necessary.

Note that full information on the approval of the study protocol must also be provided in the manuscript.